



Precipitation dynamics in southern central Asia during marine isotope stage 5: Implications for early modern human dispersal

Yue Li ^{a,h}, Yougui Song ^{a,*}, Kathryn E. Fitzsimmons ^b, Aditi K. Dave ^c, Christian Zeeden ^d, Junsheng Nie ^e, Shengli Yang ^f, Jovid Aminov ^g

^a State Key Laboratory of Loess Science, Institute of Earth Environment, Chinese Academy of Sciences, Xi'an, 710061, China

^b School of Earth Atmosphere and Environment, Monash University, Clayton VIC 3168, Australia

^c Institute of Earth Surface Dynamics, University of Lausanne, Switzerland

^d Leibniz Institute for Applied Geophysics, Stilleweg 2, 30655 Hannover, Germany

^e Key Laboratory of Mineral Resources in Western China (Gansu Province), School of Earth Sciences, Lanzhou University, Lanzhou 730000, China

^f Key Laboratory of Western China's Environmental System (Ministry of Education), College of Earth and Environmental Sciences, Lanzhou University, Lanzhou 730000, China

^g School of Mining and Geosciences, Nazarbayev University, Astana, 010000, Kazakhstan

^h Department of Chemical Engineering, University of Western Macedonia, Kozani, 50100, Greece

ARTICLE INFO

Keywords:

Central Asia
Marine isotope stage 5
Paleo-precipitation reconstruction
Westerlies
Anatomically modern human dispersal

ABSTRACT

Past warm periods provide important analogues for future warming. Marine Isotope Stage 5 (MIS 5, ~130–~70 ka) – the most recent warm interglacial – serves as a crucial testbed for evaluating potential impacts of future climate change on Central Asian hydroclimate, yet high-resolution precipitation records from this vast region remain exceptionally sparse. Consequently, the mechanisms governing MIS 5 moisture variability across Central Asia (CA), and their broader implications for ecosystem dynamics and early human dispersals, are still poorly resolved. This study reconstructed precipitation variability in Tajikistan, southern CA, during MIS 5, using principal component analysis of multiple paleoclimatic proxies preserved within loess deposits. The results reveal that the precipitation pattern in southern CA differs markedly from those in other parts of Eurasia. We investigated the likely factors influencing the difference using Convergent Cross-Mapping (CCM), and identified a fundamental transition around 102 ka for precipitation dynamics in southern CA, moving from a predominantly westerlies-forced state to a regime limited by moisture availability in source regions. Temperature-driven atmospheric moisture emerged as the primary determinant. Our findings offer valuable insights into near-future climate scenarios in southern CA, such as a likely regional increase in rainfall. Based on the MIS 5 precipitation reconstruction, we argue that the dominance of cold-season precipitation in southern CA may have impeded the northward migration of anatomically modern human (AMH) during MIS 5 north of the Central Asian mountains. We therefore recommend incorporating precipitation seasonality into simulations of AMH dispersal as a factor influencing dispersal routes and timing.

1. Introduction

Drylands are global hotspots for future warming, with critical flow-on effects for socioeconomic and ecological systems. Central Asia (CA), one of the world's largest non-zonal drylands and situated at the crossroads of major Northern Hemisphere climate subsystems, is a particularly acute case. The region exhibits greater vulnerability to climatic changes than humid regions (Huang et al., 2016). In the coming century, CA is predicted to undergo a general increase in annual

precipitation (Jiang et al., 2020) and to develop dichotomy in rainfall seasonality between the north (becoming wetter) and south (becoming drier) (Su et al., 2023). These changing distributions in precipitation patterns will affect vegetation, ecosystems, and global carbon cycle more broadly (Li et al., 2015). It remains unclear, however, whether these projected trends will deviate significantly from natural variability.

Understanding the processes governing climatic variability in CA contributes to predicting potential impact of future climate change. Since we are presently experiencing warming conditions associated with

* Corresponding author.

E-mail address: syg@ieecas.cn (Y. Song).

an interglacial, it is essential to contextualize the present and future warm climate with data from past interglacials to test model-derived hypotheses (Yin and Berger, 2015). Detailed paleoclimate reconstructions, particularly for precipitation, during the past interglacial stages, remain sparse across CA (Jia et al., 2018c; Li et al., 2020a; Lu et al., 2020). Specifically, most datasets focus on the recent Holocene interglacial (Chen et al., 2022), but with debate on the dynamics of precipitation change (Rao et al., 2019; Tan et al., 2024). Given projections that anthropogenic warming will exceed even peak Holocene temperatures and alter present-day rainfall patterns (Jiang and Zhou, 2021; Peng et al., 2019), investigation of earlier warm periods is arguably of high relevance for understanding future climate dynamics (Tierney et al., 2020). Additionally, this holds significance for examining whether the potentially asynchronous pattern of moisture changes between westerlies-dominated Asia and monsoonal Asia on (sub-)orbital timescales can be seen during past interglacial periods (Chen et al., 2019; Li et al., 2020a).

Marine Isotope Stage 5 (MIS 5, ~130–~70 ka; including the most recent interglacial) is a particularly warm phase (PAGES, 2016) which provides a useful analogue for present-day conditions (Fischer et al., 2018; Scussolini et al., 2019). There are considerable knowledge gaps in our understanding of terrestrial precipitation patterns and dynamics in MIS 5, particularly across CA. CA can be divided into northern and southern climatic provinces. Northern CA experiences spring/summer precipitation and cold, dry winters, while the south is dominated by winter/spring precipitation and hot, dry summers (Lydolph, 1977). Studies based on well dated loess-paleosol sequences indicated that there appeared to be a strong relationship between the MIS 5 moisture variability and the intensity of westerly frontal systems over precessional timescale in northern CA (Li et al., 2018a, 2020a). Comparable datasets are lacking for the southern CA region, and consequently mechanism of moisture variation during MIS 5 in southern CA remains poorly constrained. Long-term transient models have suggested that MIS 5 annual precipitation variations in the winter-rain-dominant regions of (southern) CA were dominated by primary precessional cycles (Li et al., 2013), but so far, published records from southern CA seldom align with those simulation results, especially for MIS 5d (Ding et al., 2002; Häggi et al., 2019; Lu et al., 2020). This discrepancy may be attributed to a scarcity of systematic proxy studies on MIS 5.

MIS 5 is also a period of significance since it represents an important window for anatomically modern human (AMH) dispersal out of Africa and into Eurasia (Ao et al., 2024; Beyer et al., 2021; Timmermann and Friedrich, 2016; Timmermann et al., 2022). Archaeological, genetic and fossil evidence indicates that AMH undertook multiple dispersals out of Africa during MIS 5, arriving into the Levant, southern and southeast Asia, and as far away as China (but not Europe) over this time (Demeter et al., 2012; Liu et al., 2010, 2015; Michel et al., 2016; Petraglia et al., 2007; Westaway et al., 2017). MIS 5 dispersal out of Africa is hypothesized to have been promoted by environmental stress in southeast Africa and comparatively favorable climates across Eurasia (Ao et al., 2024; Timmermann and Friedrich, 2016; Timmermann et al., 2022). Although AMH indisputably dispersed into China through northern CA during later time periods, e.g., MIS3 (Fitzsimmons et al., 2017; Zwyns et al., 2019), the early route into China – especially the mountain corridors of southern CA – remains unclear. It nevertheless has been argued that CA likely provided a crucial link in the dispersal of AMH from their African origins into East Asia, during MIS 5 (Ao et al., 2024; Asmerom et al., 2018) and also during later periods, by virtue of the climatically and ecologically favorable niche provided by the Inner Asian Mountain Corridor (Glantz et al., 2018). Clearly it is of relevance to our understanding of AMH dispersal to provide robust paleoclimatic frameworks for CA to elucidate the ecological niche hypotheses. Despite the potential significance of the CA region for early AMH dispersal, our understanding of impacts of MIS 5 conditions in the southern CA mountain corridor on the dispersal remains poorly understood.

The southern Tajikistan hosts substantial piedmont loess deposits

(Shackleton et al., 1995); these are thick sediment archives spanning long time-scales and offering a wealth of paleoclimatic information for southern CA (Ding et al., 2002; Zan et al., 2022, 2024), particularly paleo-precipitation change in this region. Therefore, numerous studies have been performed on stratigraphy (Ding et al., 2002; Dodonov and Baiguzina, 1995; Zan et al., 2022), chronology (Buylaert et al., 2024; Challier et al., 2024; Frechen and Dodonov, 1998; Gao et al., 2019; Wang et al., 2018a; Yang et al., 2020b; Zan et al., 2022), and paleoclimate proxies (Dodonov et al., 2006; Forster and Heller, 1994; Häggi et al., 2019; Jia et al., 2018c; Li et al., 2024; Lu et al., 2020; Ning et al., 2023; Schneider et al., 2025; Újvári et al., 2024; Wang et al., 2024; Yang et al., 2006; Yang and Ding, 2006) of loess in southern Tajikistan. In this paper, we undertook multi-proxy analysis of a loess section at Chashmanigar in southern Tajikistan (Fig. 1a and b) to reconstruct orbital-scale precipitation changes during MIS 5 in southern CA. We also compared these with published loess records spanning the last 30 kyr from the region (Tian et al., 2021; Yang et al., 2020b) to provide an auxiliary explanation for the dynamics of the precipitation changes. The reconstruction not only enhances our understanding of how precipitation changes in southern CA respond to external forcings and internal variabilities, but also provides insights into early AMH dispersal through Asia.

2. Methods

2.1. Study area, sampling and analyses

The mountainous southern Tajikistan is located in southern CA, with the westerly circulation as the dominant pathway for moisture transport to the region. It has a typical continental climate (Jia et al., 2018c), and receives relatively high mean annual precipitation (MAP, ~800 mm) compared with other parts of CA (generally <100–300 mm) (Song et al., 2021). This is due to the orographic uplift of moisture-laden westerly winds when they meet the South Tianshan and western Pamir Mountains (Smalley et al., 2005). As a result, the windward side of the western Pamir Plateau emerges as a “wet island” within an otherwise arid region. Precipitation in southern Tajikistan peaks during winter and spring (Fig. 1a), primarily due to the orographic uplift over the Iranian Plateau (Sha et al., 2023). This results in a pronounced seasonal contrast, characterized by cold and wet winters and springs, in contrast to hot and dry summers, indicative of a Mediterranean-type climate (Gao et al., 2019; Li et al., 2016). The Subtropical High moves into Tajikistan in summer with the onset of the Indian summer monsoon (ISM). Observations for the period 1949–1994 from the Hovaling station (13 km from the study site) show a mean annual temperature (MAT) of 11.5 °C, with the highest temperatures in July, and a MAP of 1005 mm, peaking in March (Fig. 1a).

The Chashmanigar-B (CMG-B) section (69°49'54.66" E, 38°23'18.9" N; 1549 m a.s.l) is located in the Tajik-Afghan depression of southern Tajikistan which is bordered by the Tianshan Mountains to the north and northeast, the western Pamirs to the east and the Hindu Kush Mountains to the south (Fig. 1a). The section studied here is located 20 m south of the previously published Chashmanigar section (Ding et al., 2002). CMG-B is a 25-m-thick sequence (Fig. 1b) exposed by gravitational sliding. Stratigraphic correlation with the palaeomagnetically dated, orbitally tuned Chashmanigar section (Ding et al., 2002) suggests that CMG-B spans the last full glacial cycle, MIS 5 to MIS1. A distinct reddish-brown paleosol layer occurs at 17.5–24.75 m and is assumed to correspond to MIS 5 (Li et al., 2022).

We continuously sampled the entire CMG-B profile at 2 cm intervals, following removal of superficially weathered materials. In the laboratory, we analyzed grain size (363 samples) and magnetic susceptibility (363 samples) at 2 cm intervals, soil color (181 samples) at 4 cm intervals, and total organic carbon (TOC, 60 samples) and quartz crystallinity index (QCI, 52 samples) at 12 cm intervals. Measurements followed the routine methods described below, taking place at the State

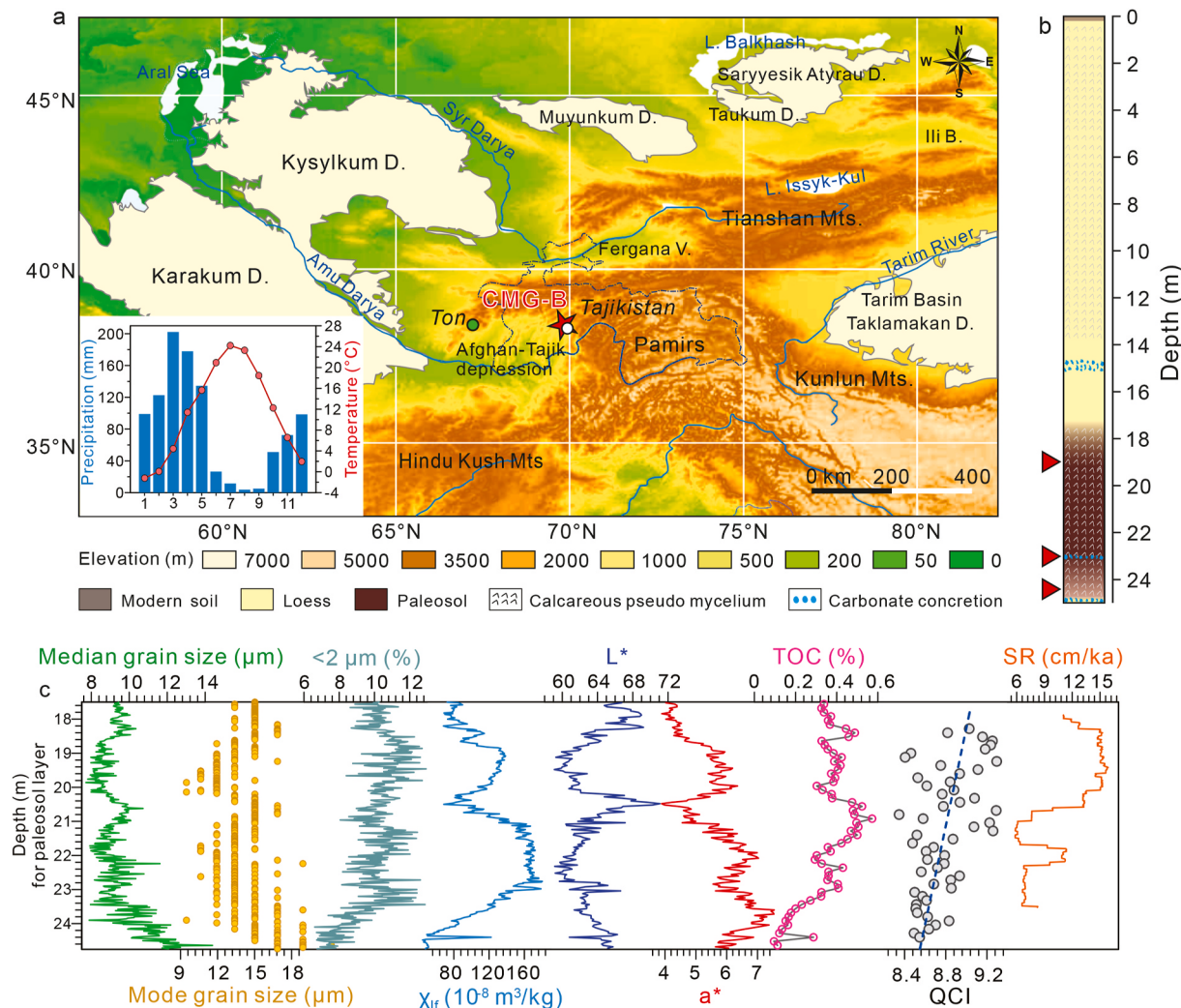


Fig. 1. (a) Locations of the Chashmanigar-B (CMG-B) loess section (red star) in southern Central Asia (CA) and the Tonnel'naya (Ton) cave site (green circle, Cheng et al., 2016). Insert shows monthly precipitation and temperature variations at Hovaling town (white circle) for the period 1949–1994 (data source: <https://www.ncdc.noaa.gov/data-access>). (b) Stratigraphic log of CMG-B with positions of luminescence samples (red triangles). (c) Variations in sediment properties within the MIS 5 paleosol at CMG-B [left-right: median grain size, modal grain size, $<2 \mu\text{m}$ fraction, low-frequency magnetic susceptibility (χ_{lf}), lightness (L^*), redness (a^*), total organic carbon (TOC), quartz crystallinity index (QCI), and sedimentation rate (SR)]. (For interpretation of the references to color in this figure legend, the reader is referred to the Web version of this article.)

Key Laboratory of Loess Science, Institute of Earth Environment, Chinese Academy of Sciences. The datasets of the loess layer (0–17.5 m) have been published (Li et al., 2024). Here, the proxies of the paleosol layer are investigated.

2.1.1. Grain size

The grain size distribution (GSD) was analyzed at 2 cm intervals, following Lu and An (1997): 0.3 g of dry bulk sample was pretreated with 30 % H_2O_2 and 10 % HCl to remove organic matter and carbonate, respectively. The treated samples were then suspended in deionized water, dispersed with 10 mL 10 % $(\text{NaPO}_3)_6$ solution and sonicated for 10 min in an ultrasonic bath to ensure complete disaggregation. The GSD was analyzed using a Malvern 3000 laser instrument. Mie theory was used to obtain the relationship between particles size and light intensity distribution pattern. Water was used as the dispersant, with a refractive index (RI) = 1.33 at 20 °C. When calculating particle size distributions with Mie theory (Grehan and Gouesbet, 1979; Wiscombe, 1980), the default refractive (1.52) and absorption (0.1) indices were applied.

Replicate analyses indicated an analytical error of <2 % for the mean grain-size. The particle size distribution was calculated for 100 grain size

classes within a measuring range of 0.02–2000 μm . Grain size parameters were calculated from the analytical data with the grain size distribution and statistics (GRADISTAT) package (version 4.0) (Blott and Pye, 2001).

2.1.2. Magnetic susceptibility

Magnetic susceptibility was measured at 2 cm intervals with a Bartington MS2 meter (Bartington Instruments, Oxford, England). Samples were oven-dried at 40 °C for 24 h. Subsample of 10 g from each sample was then precisely weighed for the magnetic susceptibility measurements. Low-frequency (0.47 kHz, χ_{lf}) and high-frequency (4.7 kHz, χ_{hf}) magnetic susceptibilities were measured. Frequency-dependent magnetic susceptibility was defined and calculated as $\chi_{fd}\% = [(\chi_{lf}-\chi_{hf})/\chi_{lf}] \times 100\%$.

2.1.3. Color reflectance

Measurements of soil color were performed on the samples collected at 4 cm intervals. Samples were ground to <74 μm (<200 mesh) before measurements, which can minimize impacts of grain size on color reflectance. We employed a portable Minolta CM-700d Spectrophotometer to measure color reflectance (Li et al., 2020b). The reference

illuminant CIE D65 was used as the light source, and the observer angle was 10°. Given the heterogeneity of the soil samples, the largest measuring port available in the spectrophotometer (with an 8 mm-diameter circular area) was selected, and the ‘specular component excluded’ (SCE) mode was then adopted to avoid glistening. The D65/10° Illuminant/Observer mode was used to record the CIE L*a*b* color data, and reflectance spectrum data were also output with a resolution of 10 nm in the range from 360 to 740 nm. L* represents the degree of lightness between black (0) and white (100), while a* and b* indicate the red-green and yellow-blue chromaticity, respectively. +a* indicates red, while -a* indicates green. +b* represents yellow, while -b* represents blue.

Each sample was measured three times and the results were averaged. After calibration with the manufacturer-recommended black and white standard tiles, repeated measurements of L*, a*, b* values for a single sample were reproducible within a ±1 % error.

2.1.4. Total organic carbon

The experimental analyses of TOCs for the CMG-B loess sediments were mainly based on the method summarized by Bisutti et al. (2004). The TOC contents (%) were measured by the soli TOC cube analyzer (Version April 18, 2017, *Elementar Analysensysteme GmbH*). The detailed experimental steps are as follows. i) Sample preparation: Grinding the loess sample into a powder and sieving the particles with a diameter less than 0.15 mm. ii) Sample treatment: Placing the grinded sample in an oven and drying it to a constant weight at 105 °C. iii) Sample combustion: Placing the dried sample in the soli TOC cube analyzer and conducting combustion analysis. During the analysis, organic matter in the sample is oxidized into CO₂ and H₂O, releasing energy. iv) Measurement of CO₂ concentration: Measuring the CO₂ concentration produced by the combustion using an infrared detector. v) Calculation of TOC content: Calculating the organic carbon content of the sample based on the CO₂ concentration. Finally, the TOC contents of the loess samples were calculated based on the sample mass and organic carbon content. The corresponding analytical error was less than 0.1 %.

2.1.5. Quartz crystallinity index

A total of 52 QCI samples were selected from the CMG-B section. Five grams of each sample were treated with 30 % H₂O₂ and 30 % HCl to remove organic matter and carbonate. The QCI was measured following Li et al. (2022), using X'pert Pro MPD X-ray diffractometer (XRD). Powders were placed in the glass holder and irradiated with a Cu Kα source with voltage at 40 kV and 40 mA. The scanning angle ranged from 67° to 69° (20), with a scan speed of 0.01° s⁻¹ and a step speed of 25.0 s. The QCI was calculated using the equation (Murata and Norman, 1976):

$$CI = F \times (a/b) \quad (1)$$

where the correction factor F is estimated at 12.24; a refers to the difference between crest value at 67.74° (20) and valley value at 67.84 (20); b is the difference between crest value at 67.74° (20) and background value. Absolute error of multiple measurements of QCI for standard quartz sample (CI = 10) is ±0.15. Here, the F value adopted herein was taken from Zhao et al. (2012). It was derived from more than five replicate analyses of a standard sample (CI = 10), which is a 1 : 1 (mass ratio) mixture of industrial-grade high-purity quartz and silicon powder. All the measurements were conducted on an XRD identical in model to the instrument used here. The F value was calculated as 10 divided by the ratio of the measured a and b values in the standard sample.

2.2. Chronological framework

We established a chronological framework for the hypothesized MIS 5 paleosol at CMG-B using polymineral post-IR IRSL (pIR₂₀₀IR₂₉₀) dating

on samples collected at 19 m, 23 m and 24.4 m depths (Fig. 1b). By combining the ages with correlation of median grain sizes with the ice volume record (Grant et al., 2012), we developed a Bayesian age-depth model using BACON 2.2 (Blaauw and Christen, 2011) (Fig. 2). Previous work at Chashmanigar demonstrated that grain-size variations in Tajik loess profiles correlated with global ice volume changes (Ding et al., 2002), forming the basis of our relative age model.

On the one hand, the pretreatments and measurements of the three luminescence samples were performed in a dim red-lit darkroom at the luminescence laboratory of the Key Laboratory of Western China's Environmental Systems (Ministry of Education) of Lanzhou University. Both the outer ~5 cm and the inner tube material of each tube sample were split in two parts. The outer 5-cm ends of the tube samples were used to determine water content and radioactive elements. The inner material was treated with 30 % H₂O₂ and 10 % HCl to remove organic matters and carbonates, respectively. The treated samples were settled in deionized water according to Stokes' Law to retrieve the 4–11 μm polymineral fraction.

Luminescence signal measurements were made using an automated Risø TL/OSLDA-20 reader equipped with blue LRDs (470 nm, ~80 mW/cm²) and IR LEDs (870 nm, ~135 mW/cm²). Laboratory irradiation was conducted by using a ⁹⁰Sr/⁹⁰Y beta source installed in the reader. A pIR₂₀₀IR₂₉₀ dating protocol was applied. The first infrared stimulation was carried out at 200 °C for 200 s, followed by a second IR stimulation at 290 °C of the same duration (Buylaert et al., 2012; Li and Li, 2012; Thiel et al., 2011a). The IR signals obtained on stimulation of feldspar in the polymineral fine grains was detected using a Blue Filter that combines a 4 mm Corning 7-59 with a 2 mm Schott BG39. The pIRIR signal was calculated from the first 2 s of the decay curve after subtraction of the average taken from the last 20 s. For each sample, 8 aliquots were measured by the pIR₂₀₀IR₂₉₀ protocol, and a test dose of 30–50 % of the measured equivalent dose (D_e) was utilized (Li and Li, 2012). All polymineral pIR₂₀₀IR₂₉₀ dose response curves were fitted using a single exponential plus a linear function in the Analyst v4.57 software package (Duller, 2015), and the final D_e values were evaluated using the Central Age Model (Galbraith et al., 1999).

Environmental dose rates were derived from the geochemically determined concentrations of radioactive elements in each sample. The concentrations of uranium (U), thorium (Th), and rubidium (Rb) were measured using inductively coupled plasma mass spectrometry (ICP-MS), while potassium (K) contents were determined through inductively coupled plasma optical emission spectroscopy (ICP-OES) at Xi'an Geological Survey Center, China. External dose rates of the polymineral samples were calculated based on radioactive element concentration and conversion factors described by Guérin et al. (2011). Cosmic dose rates were calculated based on altitude and location of the sample, according to equations given by Prescott and Hutton (1994). The internal dose rate of the fine-grained K-feldspar was estimated based on an assumed K content of 12.5 ± 0.5 % (Huntley and Baril, 1997) and a Rb content of 400 ± 100 ppm (Huntley et al., 2001). Feldspar internal dose rates include a small internal dose rate contribution of 0.06 ± 0.03 Gy/ka from U and Th (Mejdahl, 1987; Zhao and Li, 2005; Stevens et al., 2018). Water content for each sample was calculated by determining the weight before and after drying the sample and then dividing their mass difference by the mass of the dry sample. Total environmental dose rates and the corresponding ages were calculated using the Excel-based Luminescence Dose and Age Calculator (LDAC) (Liang and Forman, 2019).

On the other hand, our recent studies have indicated that the CMG-B loess comprises floating dust and fine-grained dust transported by westerlies (Li et al., 2022, 2024). As the westerly-transported component corresponds to a persistent and stable background dust with a virtually invariant grain size (modal size of ~10 μm) (Gu et al., 2020; Vandenberghe, 2013; Wu et al., 2006), variations in loess grain size are governed primarily by the relative abundance of the floating dust. Floating dust still stems from dust storms (Lin et al., 2016), which shows

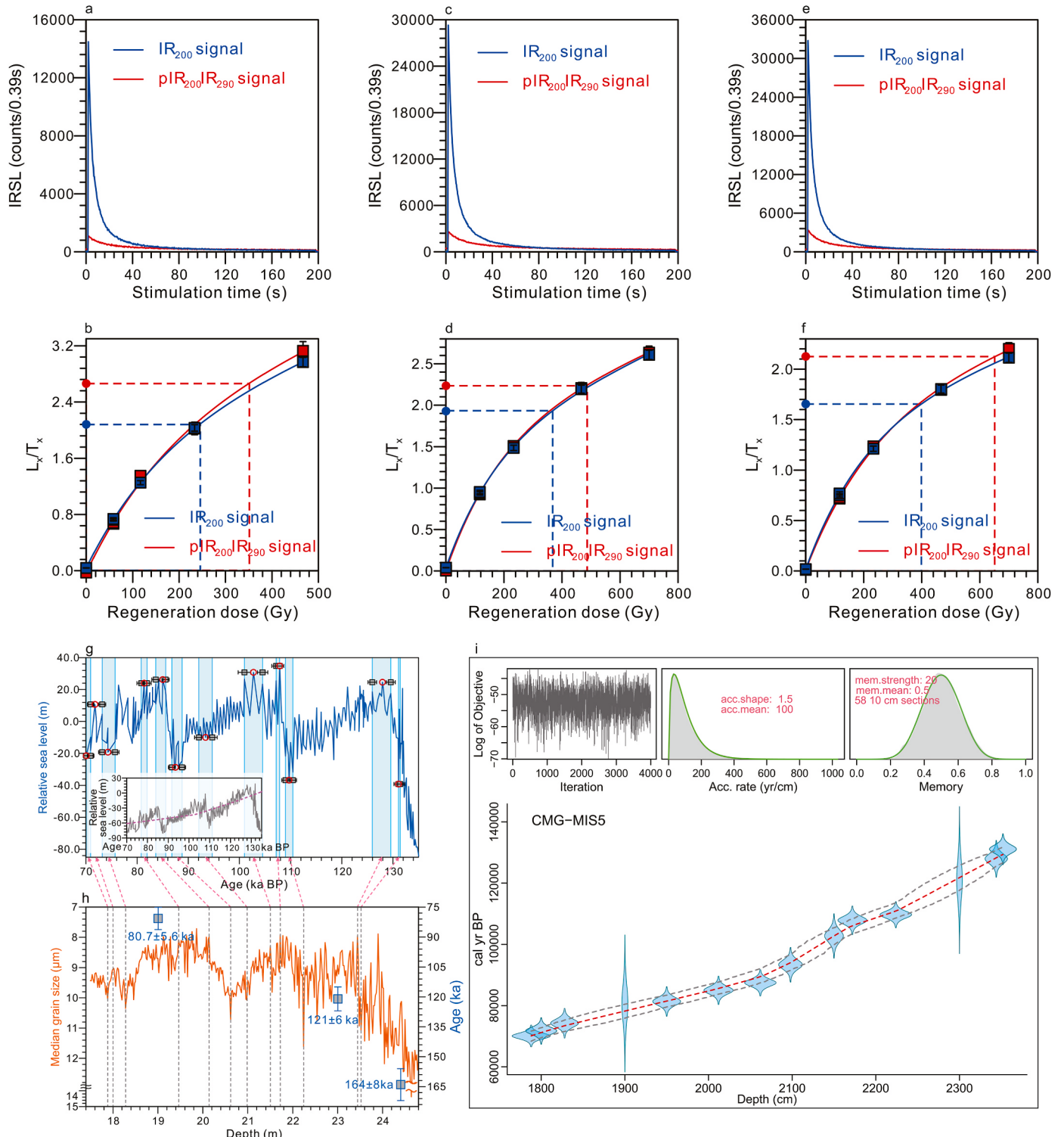


Fig. 2. (a, c, e) Decay curves for aliquots from the luminescence samples at depths of 19 m, 23 m, and 24.4 m in the CMG-B section. (b, d, f) Dose-response curves of these luminescence samples. (g, h) The relative sea level (Grant et al., 2012) and the median grain sizes of the CMG-B section were compared to identify the tie points for establishment of the age-depth relationships of the paleosol layer (17.5–24.75 m). The pink dotted line in the inset of (g) shows the long-term trend of the relative sea-level record, derived from locally weighted regression analysis. (i) Bayesian age-depth model of the paleosol layer (dotted red line indicates weighted mean age), underlying the distributions of individual polymineral post-IR IRSL ($\text{pIR}_{200}\text{IR}_{290}$) luminescence ages and tie points (blue), with 95 % probability intervals (gray shaded area). The three small panels show time series of the log-posterior for the subsampled Markov Chain Monte Carlo (MCMC), prior (green) and posterior (gray) for accumulation rate (yr/cm) with $\text{acc.shape} = 1.5$ and $\text{acc.mean} = 100$, and prior and posterior for memory, with $\text{mem.strength} = 20$ and $\text{mem.mean} = 0.5$. Model resolution is 10 cm, which produces 58 sections for the range of dated depths. (For interpretation of the references to color in this figure legend, the reader is referred to the Web version of this article.)

no general correlation with wind strength (Qiang et al., 2010). Consequently, proportion of the floating dust in the CMG-B loess deposits was thought to reflect dust storm frequency rather than wind strength. As dust storm frequency reduced, the floating dust proportion and correspondingly the CMG-B loess grain size decreased, but with almost consistent minimum values due to increased dominance of the background dust. Global ice volume changes provided major atmospheric dynamics for occurrence of dust storms in the Tajik-Afghan depression by controlling the Caspian Sea-Hindu Kush Index (CasHKI) mode, which operated through modulating the differences in sea-level pressure between the Caspian Sea and Hindu Kush/Pamirs (Li et al., 2019b, 2024). This in turn confirms the linkage between ice volume and Tajikistan loess grain size (Li et al., 2024).

We applied locally weighted regression to remove long-term trend from the relative sea-level (representing ice volume) record (Fig. 2g) using *Acycle v2.4* (Li et al., 2019a) because of the similar minimum grain sizes (attributed to dominance of the background dust) throughout the paleosol layer (Fig. 1c). Subsequently, peaks and valleys were matched between the relative sea-level record (Grant et al., 2012) and the median grain sizes of the CMG-B paleosol layer (Fig. 2g and h). Here, we considered two sources of age uncertainty: corresponding peak-to-peak and valley-to-valley matching and age model of the sea-level record. Specifically, the earliest and latest possible dates for both peaks and valleys on the sea-level curve were identified (see the light blue stripes in Fig. 2g); the new chronology of the Red Sea sea-level record used here included 2 standard errors (2σ). They were assumed to be independent. Following the strategy for estimating tie-point age uncertainty in Hobart et al. (2023), the range between earliest and latest ages for each identified peak or valley was assumed to represent a 95 % confidence interval, approximately one-quarter of which was equal to a standard deviation. Finally, the square root of the sum of squared standard deviations was calculated as the standard deviation of the total tie-point age uncertainty.

2.3. Data analysis approaches

Since multiple factors influence on loess properties and their potential to act as proxies (see Section 4.2), we performed principal component analysis (PCA) to examine interrelationships between sediment properties and thereby to develop a reliable precipitation index. We used generalized additive model (GAM) to characterize orbital or longer-term precipitation trends considering dating uncertainties. To extract directly causality behind associations between precipitation changes and potential drivers, Convergent Cross-Mapping (CCM, Sugihara et al., 2012) was applied, instead of statistical correlation analysis. CCM can unravel causation from complex nonlinear systems such as the climate (Dima et al., 2021; Koutsoudris et al., 2023; Tsonis et al., 2015; Van Nes et al., 2015; Wang et al., 2014) based on dynamical system theory (Sugihara et al., 2012). The descriptions of the above-mentioned methods are as follows.

2.3.1. Principal component analysis

PCA is a technique utilized to simplify the complexity of high-dimensional data by projecting them geometrically onto lower dimensions (Jolliffe and Cadima, 2016, and references therein). PCA enables the interpretation of data trends and variations through a reduced number of latent variables, with minimal loss of information. This is particularly useful for extracting major paleoclimate signals from multiple paleoclimate proxies and identifying influencing factors of variations in those proxies. Through the orthogonal rotation of the covariance matrix, principal components (PCs) are generated as linear combinations of the initial variables along axes carrying most of the variance (Maćkiewicz and Ratajczak, 1993). These PCs are uncorrelated and ranked in terms of recorded quantity of information. The amount of information represented by each PC is reflected by eigenvalues, while eigenvectors display the direction of the axes carrying most of the

variance (information) in the dataset. The results of PCA are typically presented as biplots, which are two-dimensional plots depicting one PC on the x-axis and another PC on the y-axis. We conducted PCA on our proxy data to obtain the PC which can reliably indicate precipitation changes during MIS 5. PCA was performed using the *PCA* function of the “FactoMineR” package (Lê et al., 2008), and a biplot was drawn using the *fviz_pca_biplot* function of the “factoextra” package (Kassambara and Mundt, 2017), in R environment (R Core Team, 2019).

2.3.2. Smoothing processing using generalized additive model

The GAM (Hastie and Tibshirani, 1986) enables us to capture the intricate patterns and non-linear relationships within our data, resulting in more accurate trend forecasting. Here, the GAM smoothing function was fitted to the time series of the precipitation index, the Gulang loess mean grain size, the sea surface temperatures in the North Atlantic and the Bay of Bengal, and the CO₂ concentration to emphasize their variations at the orbital timescale. In this procedure, the complexity of the fitted smoothing function was objectively determined through automatic selection, thereby ensuring a reproducible approach to data smoothing. We ran the GAM model in R environment (R Core Team, 2019). The *gam* function of the “mgcv” package (Wood and Wood, 2015) was employed to perform the GAM smoothing. Thereinto, the spline-based smooths were used to help set up the GAM model, and correspondingly the basis function (k), the dimension of the basis used to represent the smooth term, was set to the default value. Generalized cross-validation was employed to automatically select the smoothing parameter.

2.3.3. Convergent cross-mapping

The CCM analysis is derived from the Takens' Theorem (Deyle and Sugihara, 2011; Takens, 1981), which states that in a dynamical system characterized by the influence of timeseries variable A on timeseries variable B, the state of A at time t can be accurately predicted from the state of B at time t. CCM analysis can discern causality from simple correlation in multivariate timeseries from deterministic dynamical systems (Runge et al., 2019; Sugihara et al., 2012). This is achieved by evaluating the degree to which variable B, influenced by variable A, can accurately infer the states of the causal variable A – a metric referred to as “CCM skill” (ρ) (Sugihara et al., 2012). Since true (whether direct or indirect) causation is identified by convergence from simple correlations in the CCM analysis, the accuracy of the cross-mapped forecasts, indicated by the ρ value, improves with the expansion of the time series utilized to project variable A based on variable B.

The time-delayed CCM is also applied to further determine the true direction of causality and identify a potential occurrence of dynamic synchrony (i.e., two variables are forced by a third variable) (Koutsoudris et al., 2023; Van Nes et al., 2015; Ye et al., 2015). Negative time displacements that result in increased ρ values would suggest a genuine causal effect, provided there is a difference in the optimal lag between the CCM skills of one variable to the other. Conversely, positive time displacements would indicate that the affected variable is more effective at predicting future values of the driving variable, thereby allowing for the exclusion of causality (Ye et al., 2015).

In this study, we first evaluated the system's nonlinearity with the S-map procedure introduced by Sugihara (1994). This method reconstructs the underlying dynamics by fitting locally linear maps whose influence radii are modulated by a nonlinearity parameter θ that weights neighboring phase-space points during estimation (Wang et al., 2018c). Forecast skill ρ peaking at $\theta = 0$ indicates linear dynamics, whereas ρ rising with θ confirms nonlinearity. The S-map test was conducted using the *PredictNonlinear()* function in the “rEDM” package (version 1.15.4) (Ye et al., 2018). CCM was performed using the *CCM()* function of the “rEDM” package (version 1.15.4) (Ye et al., 2018) in R environment (R Core Team, 2019). All datasets were interpolated linearly to equidistant 0.5 ka time steps prior to CCM analysis. Optimal CCM prediction parameters (i.e., the optimal combination of embedding dimension E and

lag of time delay embedding τ) that can yield the highest ρ values were determined by running the *Simplex()* function included in the “rEDM” package multiple times, based on the entire timeseries that were split into library and predictor variables. For our datasets, a range of 1–10 for E and 1–4 for τ were examined, and $E = 3$ and $\tau = 2$ were utilized as the optimal parameters. The visualization of correlation between cross-mapped and observed values as a function of the timeseries length (library size) were conducted using the R function *CCM.boot* function from the “multispatialCCM” package (Clark et al., 2015). Time-delayed CCM was performed using the *CCM()* function of the “rEDM” package (version 1.15.4) (Ye et al., 2018) by setting the $T_p(\tau)$ parameter to ± 30 (0.5 ka each). The R codes for the CCM analysis are available in Supplementary Text 1.

3. Results and discussions

3.1. Age model for the paleosol layer

The decay and growth curves for pIRIR₂₉₀ (post-IR IRSL) and IR₂₀₀ signals of the luminescence samples are shown in Fig. 2a–f. The pIR₂₀₀IR₂₉₀ signals decay rapidly, reaching background levels within the first 40 s of stimulation. Radioactive element (U, Th, K) contents, water contents (with a 5 % uncertainty), dose rates, and D_e values are detailed in Supplementary Table 1. The corresponding pIRIR ages at 19 m, 23 m, and 24.4 m are 80.7 ± 5.6 ka, 121 ± 6 ka, and 164 ± 8 ka, respectively (Fig. 2h), increasing with depth as expected from the stratigraphic sequence.

However, it is noted that base of the observed paleosol layer (24.4 m) with an age of 164 ± 8 ka does not coincide with inception of the last interglacial. The growth curve for the sample at 24.4 m shows a calculated D_0 (natural dose, Wintle and Murray, 2006) of 644 ± 57 Gy, with D_e (648.3 ± 19.1 Gy) $< 2D_0$ (1288 ± 114 Gy). This suggests that the pIR₂₀₀IR₂₉₀ signal is below the saturation value from the laboratory dose-response curve. Previous studies using elevated temperature pIRIR protocols on feldspar reported low fading rates for the resulting pIRIR signal (Buylaert et al., 2008; Thiel et al., 2011b; Thomsen et al., 2008), leading us to consider fading minimal for our samples. Nevertheless, since the K-feldspar ages here have not been corrected for residual doses, the sample at 24.4 m may retain a high residual. Thus, we regarded this age as a maximum and exclude it from our age model. The ages for samples at 19 m (80.7 ± 5.6 ka) and 23 m (121 ± 6 ka) corroborated well with the tie points of the relative age model (Supplementary Table 1) and were included in the final age model for the MIS 5 stratigraphy (Fig. 2i). Based on the final Bayesian age model, we estimated the inception of MIS 5 in the CMG-B section to be 131 ± 1.3 ka.

Sedimentation rate (SR) of the MIS 5 paleosol layer varies from 6 to 16 cm/ka, averaging 11 cm/ka. This rate is comparable to those obtained at the Kuldara section (~11 cm/ka, Buylaert et al. (2024)), the Darai Kalon section (~9 cm/ka, Häggi et al. (2019)), and the Chashmanigar section (~10 cm/ka, Ding et al. (2002)), all in close proximity to the CMG-B section. The consistent SR potentially corroborate our age model.

3.2. Interpretation of the paleoclimatic proxies

3.2.1. Grain size

The paleosol layer is dominated by silt, ranging from 88.4 % to 93.0 % (averaging 90.4 %), and the GSDs show primary modal peaks at 10–19 μm (Fig. S1a). Based on the interpretations of modal grain sizes (Fig. 1c) and the end-member modeling of GSDs (Li et al., 2022, 2024), we suggested that the CMG-B loess was comprised of floating dust and westerly-transported fine particles, and the loess grain-size variations mainly reflected dust storm frequency (see Section 2.2). The CasHKG mode probably provided major atmospheric dynamics for dust storms in the Tajik-Afghan depression (Li et al., 2019b), which controlled the variations in Tajikistan loess grain size (Li et al., 2024). The median

grain sizes of the paleosol layer range from 7.7 μm to 14.4 μm , with a mean of 9.4 μm . Noticeable decreases in the median grain size were observed at 18.6–20.2 m, 21.2–2.2 m, and 23.0–23.6 m (Fig. 1c), indicating reduced frequency of dust storms during those corresponding periods.

The <2 μm fraction contents of the paleosol layer range from 6.6 % to 12.9 %, with high-frequency fluctuations (Fig. 1c). The <2 μm fractions of loess deposits were commonly found to have a strong correlation with pedogenesis (Bronger and Heinkele, 1990; Sun et al., 2011a), which were used to indicate regional moisture changes (Gao et al., 2022; Jia et al., 2018b). However, GSD is a closed number space, and changes of the <2 μm fractions are largely determined by variations in coarse fractions due to lower frequency of the former in loess deposits (i.e., dilution effect) even if their contents are associated with intensity of pedogenesis. For example, grains larger than ~20 μm , originating from proximal dust sources, display a negative correlation ($r = -0.52$) with the <2 μm fractions in the CMG-B paleosol layer. Therefore, although the <2 μm fraction has been considered as a potential indicator of pedogenesis intensity and precipitation change, its validity has to be examined.

3.2.2. Magnetic susceptibility

The χ_{lf} varies from 44.6 to $180.4 \times 10^{-8} \text{ m}^3 \text{ kg}^{-1}$, with an average of $119.3 \times 10^{-8} \text{ m}^3 \text{ kg}^{-1}$. Typically, $\chi_{\text{fd}}\%$ indicates concentrations of fine-grained magnetic particles forming in situ during soil pedogenesis (Liu et al., 2012; Maher and Taylor, 1988; Zhou et al., 1990). The $\chi_{\text{fd}}\%$ values of the CMG-B paleosol layer vary in 2.0–9.5 % (averaging 7.0 %), except for two samples at 22.9 m and 24.5 m yielding $\chi_{\text{fd}}\%$ values of 1.6 % and 1.9 %, respectively. It reflects a coexistence of pedogenic superparamagnetic ferrimagnetism and detrital coarser ferromagnetic materials according to the criteria of Dearing (1999). However, pedogenic magnetic signal detected by superparamagnetic ferromagnetic materials remains distinct, as their magnetic susceptibility values are 2–3 times greater than those of detrital coarser grains. Moreover, weathering and dissolution of pedogenic magnetic minerals under anoxic conditions attributed to waterlogging (Liu et al., 2013; Maher, 1998) are not observed (Fig. S1b). Loess magnetic susceptibility has also been suggested to be strongly affected by dilution effect of dust sedimentation rate (Kong et al., 2020). However, variations in the magnetic susceptibility and the SR are asynchronous throughout the paleosol layer (Fig. 1c), implying no significant dilution effect. Therefore, the magnetic susceptibility variabilities of the CMG-B paleosol layer are related primarily to post-depositional pedogenesis (Fig. S1b). Based on the systematic investigations of magnetic minerals, Jia et al. (2018c) suggested that magnetic susceptibility enhancement of the Tajikistan loess was intimately associated with pedogenesis, which has been used to indicate intensity of pedogenesis controlled by moisture availability (Fan et al., 2021; Lu et al., 2020; Wang et al., 2018b).

Kang et al. (2020) suggested that MAP, as opposed to MAT, held the predominant influence over the magnetic enhancement observed in surface soils in Tajikistan. Since pedogenic fine-grained magnetite/maghemite is primarily formed during wet season, instead of throughout entirety of the year (Yang and Jia, 2021), Tajikistan loess magnetic susceptibility mainly records the winter/spring precipitation signal (Fan et al., 2021). The χ_{lf} results of the CMG-B paleosol layer show marked variabilities, with higher values at 18.8–20 m and 21–23 m (Fig. 1c) indicative of increased winter/spring precipitation during those corresponding periods.

3.2.3. Colorimetry

The lightness (L^*), ranging from 59.1 to 71.1, is in inverse proportion to the χ_{lf} (Fig. 1c). Loess L^* is mainly affected by pedogenic elements, such as iron oxides (darkening the soil color), organic matter (darkening), and CaCO_3 (lightening) (Ji et al., 2001; Sun et al., 2011b). Chen et al. (2016) and Jia et al. (2018a) have used loess L^* as a proxy for reconstructing rainfall changes in CA, attributed to influence of organic

matter concentration (Yang et al., 2001). However, a significantly opposite relationship was not found between the L^* and the TOC (Fig. 1c; $r^2 = 0.00005$). The redness (a^*) inversely shows generally inverse trends to the L^* (Fig. 1c). Typically, a^* reflects the extent of coloration mainly caused by hematite (Chen et al., 2010; Jiang et al., 2022; Meng et al., 2021; Sun et al., 2011b; Torrent et al., 1983). However, given the lower mass contents of hematite relative to CaCO_3 contents in the Tajikistan loess (Häggi et al., 2019; Jia et al., 2018c), CaCO_3 contents appeared to dominate variations in the L^* in this study, with low CaCO_3 contents due to increased precipitation and strong eluviation (Li et al., 2020a) resulting in low L^* values.

The a^* , with a range of variation between 3.89 and 7.54, gradually increases down the paleosol, albeit with large fluctuations, and reaches its maximum value at 23.6 m (Fig. 1c). Previous study regarded a^* as a rapid and non-destructive proxy for weathering intensity of loess deposits (Yang and Ding, 2003). In the Ili Basin, northern CA, the strong redness in the loess-paleosol sequences indicated a relatively moist climate condition (Yang et al., 2020a). However, redness of terrestrial sediments may be also controlled by temperature (Li et al., 2018b; Wang et al., 2013; Zhang et al., 2014), and degree of reddening in loessic soils indicated soil temperature (Gao et al., 2018, 2024; Guo et al., 2009; Jia et al., 2018c). Therefore, it reasonably suggests that precipitation changes cannot be exclusively reconstructed by loess a^* alone (Ji et al., 2001, 2004).

3.2.4. Total organic carbon

The TOC content, varying in 0.10–0.57 % with an average of 0.35 %, fluctuates around a mean value of 0.40 % at 17.5–23 m, and significantly reduces at 23–24.6 m (Fig. 1c). TOC is mainly derived from degradation of the overlying vegetation (Babesh et al., 2017; Cerling et al., 1989; Jia and Lin, 1993; Rao et al., 2013; Zaady et al., 2001); thus, TOC contents in aeolian deposits from the arid and semiarid regions are associated with vegetation cover and biomass (Lu et al., 2013, 2019; Xiao et al., 2002; Yin et al., 2016). Rodrigueziturbe et al. (1999) suggested a coupled relationship between TOC content, vegetation cover and humidity. Hence, higher TOC contents indicated increases in effective moisture and vice versa (Lu et al., 2012; Miao et al., 2007, 2020; Shi et al., 2003). Nevertheless, in their study of the grasslands in the U.S. Great Plains, Parton et al. (1987) demonstrated that soil TOC content in a stable land surface depended on the balance between productivity of ecosystem and microbial decomposition. The decomposition of soil TOC can be accelerated by rising temperature (Fang et al., 2005; Knorr et al., 2005). Therefore, influence of temperature on soil TOC content should not be overlooked, though it was interpreted be an indicator of effective moisture.

3.2.5. Quartz crystallinity index

Fig. S1c shows the XRD patterns from 67° to 69° (20) for calculation of the QCI values. The QCI exhibits evident variabilities, ranging from 8.4 to 9.3 (averaging 8.8), with a decreasing tendency observed down the paleosol (Fig. 1c). Quartz is a ubiquitous and weather-resistant rock-forming mineral. QCI depends on types of source rocks, ascribed to temperature and crystallization rate during formation (Murata and Norman, 1976). It has been applied to identifying the sources of loess deposits on the Chinese Loess Plateau (CLP) (Ono et al., 1998; Sun et al., 2007, 2008, 2013). Our previous study indicated the slightly higher CI values of the <16 µm fraction, compared to the >16 µm fraction, in the CMG-B loess (Li et al., 2022), which may distinguish between distal and proximal sources. Therefore, QCI was employed in this study to assess the potential influences of source changes on the aforementioned proxies prior to precipitation reconstruction.

3.3. Proxy-based reconstruction of precipitation changes during MIS 5

In light of their complex interpretations as mentioned above, we conducted a PCA on these MIS 5 paleosol proxies to further examine

their validity as a precipitation proxy. The first two principal components (PC1 and PC2) explain 68.7 % of the total variance (Fig. 3a–c and Supplementary Table 2). PC1 is mainly determined by TOC, a^* , <2 µm fraction, median grain size, and QCI, while PC2 is dominated by L^* and χ_{lf} . As also shown in Fig. 3d, the biplot illustrates that L^* and χ_{lf} are near the y-axis (PC2), and other proxies are basically near the x-axis (PC1).

Variables mainly contributing to PC1 show that a^* is negatively correlated with QCI (Fig. 3d), suggesting influence of changing source on original iron oxide compositions and consequently a^* . Median grain size and <2 µm fraction exhibit a negative relationship, implying the variability in the <2 µm fraction strongly influenced by closed number space of grain size distribution or aerodynamic environment, other than pedogenic weathering. The smaller angles between the loading vectors for TOC, <2 µm fraction, and QCI (Fig. 3d) suggest the possible adsorption of organic matter onto aggregates and fine-grained minerals (Lützow et al., 2006), potentially influenced by changing source. Therefore, the considerable influences of aerodynamic environment and provenance on a^* , <2 µm fraction and TOC contents question the reliability of precipitation reconstruction based on the PC1.

PC2 displays nearly opposite loading vectors for L^* and χ_{lf} (Fig. 3d). The approximately 90° angle between the loading vectors for χ_{lf} and QCI suggests χ_{lf} variability independent of source changes. The larger angle between L^* and median grain size indicates a negligible effect of aerodynamic environment on L^* variability. The negative correlation between χ_{lf} and median grain size, indicated by their opposite loading vector directions, helps to exclude influence of wind vigor on magnetic enhancement (Fig. S1b). The nearly vertical loading vectors for L^* and TOC suggest that L^* variability is not controlled by organic matter. Although the angle between L^* and QCI loading vectors is small, the low correlation coefficient ($r = 0.27$) indicates a minor influence of source on L^* . To summarize, we interpreted PC2, primarily driven from L^* and χ_{lf} , as a precipitation change signal. χ_{lf} is a well-established pedogenic proxy for precipitation variations, and L^* reflect precipitation changes by influencing carbonate eluviation.

However, resolution of the PC score is constrained by the 12-cm interval of the QCI samples. Therefore, we combined χ_{lf} and L^* by normalizing each with Z-score normalization and averaging them into a composite precipitation index. This index presents values at 4 cm intervals, equivalent to an averaged temporal spacing of ~0.4 ka. Given chronological uncertainties and to ensure the robustness of these single-point inferences, we focused on GAM-smoothed (orbital) precipitation changes, following the approaches of Wang et al. (2022) and Van der Meeran et al. (2022). To further evaluate influences of the chronological uncertainties on the precipitation pattern, probabilistic analysis was conducted using a random walk Monte Carlo routine (5000 simulations) (details are provided in Hu et al. (2024); Supplementary Text 2). This approach incorporates a Metropolis–Hastings algorithm to reject steps in the random walk that lead to age reversals (Rodríguez-Sanz et al., 2017). The probabilistic analysis results of our precipitation index for MIS 5 show peak precipitation at ca. 80 ka, ca. 95 ka and ca. 114 ka, and significantly reduced precipitation during 70–76 ka and 86–92 ka, which are independent of MIS 5 sub-stages, particularly for MIS 5d (Fig. 4a). This pattern is also evident in the GAM-smoothed precipitation index (Fig. 4h–q). Therefore, age uncertainties do not strongly influence the pattern of orbital-scale precipitation change.

The stalagmite trace elements from Tonnel'naya (Ton) cave, Uzbekistan, 227 km west of the CMG-B section (Fig. 1a), reflect regional effective moisture changes (Cheng et al., 2016). Our probabilistic analysis results show considerable similarities in the variation trend to the stalagmite Sr/Ca ratios (Fig. 4b), validating the MIS 5 precipitation pattern demonstrated by our results. However, some observed discrepancies may be attributed to temperature effects on effective moisture variations (Tan et al., 2024). In addition, this pattern of precipitation change can also be observed in other loess sections in the Tajik-Afghan depression. Specifically, the higher χ_{fd} and χ_{lf} values in the Darai Kalon (DK) loess section indicate significantly increased precipitation during

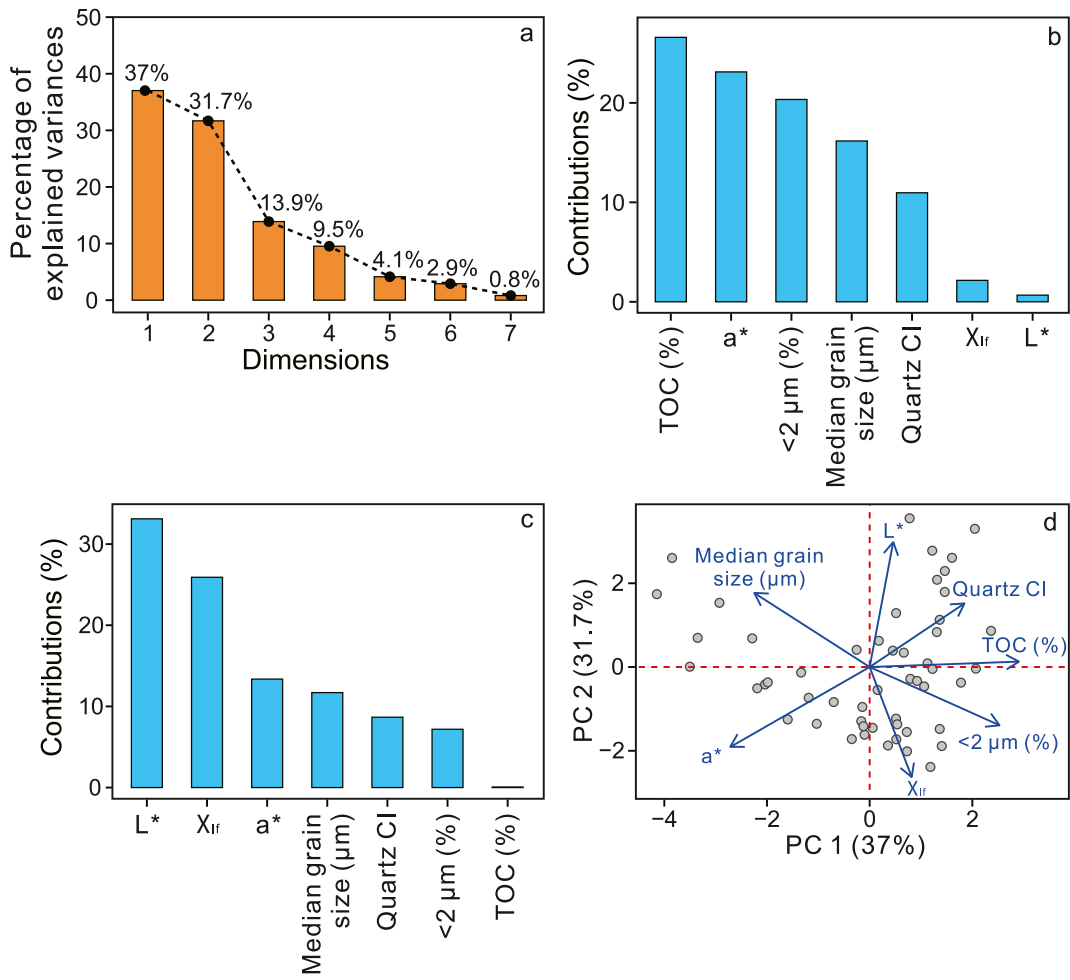


Fig. 3. (a) Scree plot showing eigenvalues of the principal components analysis (PCA) on the median grain size, $<2\text{ }\mu\text{m}$ fraction, χ_{lf} , L^* , a^* , TOC, and QCI of the paleosol layer in the CMG-B section. (b, c) Contribution of each variable to principal component 1 (PC1) and PC2, respectively. (d) Compositional biplot of multiple paleoclimate proxies of the CMG-B loess during the concerned interval.

MIS 5d; conversely, the relatively lower χ_{fd} and χ_{lf} values suggest reduced precipitation during MIS 5b, given the dating uncertainty (Jia et al., 2018c; Lu et al., 2020; Wang et al., 2024) (Fig. 4c and d). Similar characteristics can also be observed in the CaCO_3 contents of the DK section (Häggi et al., 2019) and the Rb/Sr ratios of the Chashmanigar section (Yang et al., 2006) throughout MIS 5 (Fig. 4e and f). Recently, Wang et al. (2024) conducted a $\delta^{13}\text{C}_{\text{org}}$ study of the DK section, and suggested that the loess $\delta^{13}\text{C}_{\text{org}}$ records had the potential to directly reflect paleo-precipitation variations since the last interglacial. Similar patterns of variation are also found between our precipitation index and the (negative) $\delta^{13}\text{C}_{\text{org}}$ record (Fig. 4a–g). Therefore, the precipitation index reveals a distinct precipitation pattern, characteristically prevalent across southern CA.

We investigated the spatial extent of precipitation patterns across Eurasia (see Fig. S2 for the locations of the paleoclimate records used for comparisons). In general, paleoclimatic proxies from the Mediterranean Basin and Middle East (Fig. 4i–p), the tropical Indian Ocean (Fig. 4r and s), central China (Fig. 4t), and the Chinese Loess Plateau (Fig. 4u and v), all suggest increased (reduced) precipitation during MIS 5a, c, e (MIS 5b, d). In contrast, the Ili Basin in northern CA experienced increased moisture during MIS 5b, d (Fig. 4w and x). Thus, the MIS 5 precipitation pattern in southern CA markedly differs from those in Asian monsoon regions and westerly-dominated Mediterranean, Middle East, and northern CA. As a result, precipitation drivers in southern CA cannot be entirely explained by the climatic mechanisms acting on the other regions.

3.4. Driving mechanisms of MIS 5 precipitation patterns in southern CA

Multiple drivers potentially influencing precipitation variations in CA have been identified, primarily through their effects on the behavior of the westerlies, including Northern Hemisphere ice sheet, CO_2 concentration, Siberian High, latitudinal insolation gradient, obliquity, precession, and surface temperature of water vapor source (Supplementary Text 3). However, their linear correlation coefficients with the precipitation index are relatively low, with a lack of consistent pattern of variation (Fig. 5a–i). The S-map tests in the CCM analyses indicate their nonlinear behaviors, as shown by the improved ρ with the increased θ (Fig. S3). Therefore, our datasets are well suited for CCM analysis. The CCM results show that ρ significantly improve and converge with larger library sizes (Fig. 5j–q), suggesting the causal links. However, ρ values for “precipitation maps sea surface temperature (SST) of northern Indian Ocean and CO_2 concentration (blue lines)” exceed those of the reverse mappings (red lines), indicating that these factors do not strongly causally affect precipitation. To further address potential strong coupling within the systems, time-delayed CCM was conducted (Fig. 5j–q), with non-positive optimal lag for real causality (Ye et al., 2015). We found that optimal (maximum) ρ values for CCM estimates based on precipitation displayed positive time displacements for ice volume and Siberian High (red lines), and thus argued that these drivers can be ruled out as causal factors. By contrast, optimal ρ values occur with time lags for Iberian margin SST, obliquity, and precession, demonstrating their unidirectional forcings on precipitation changes.

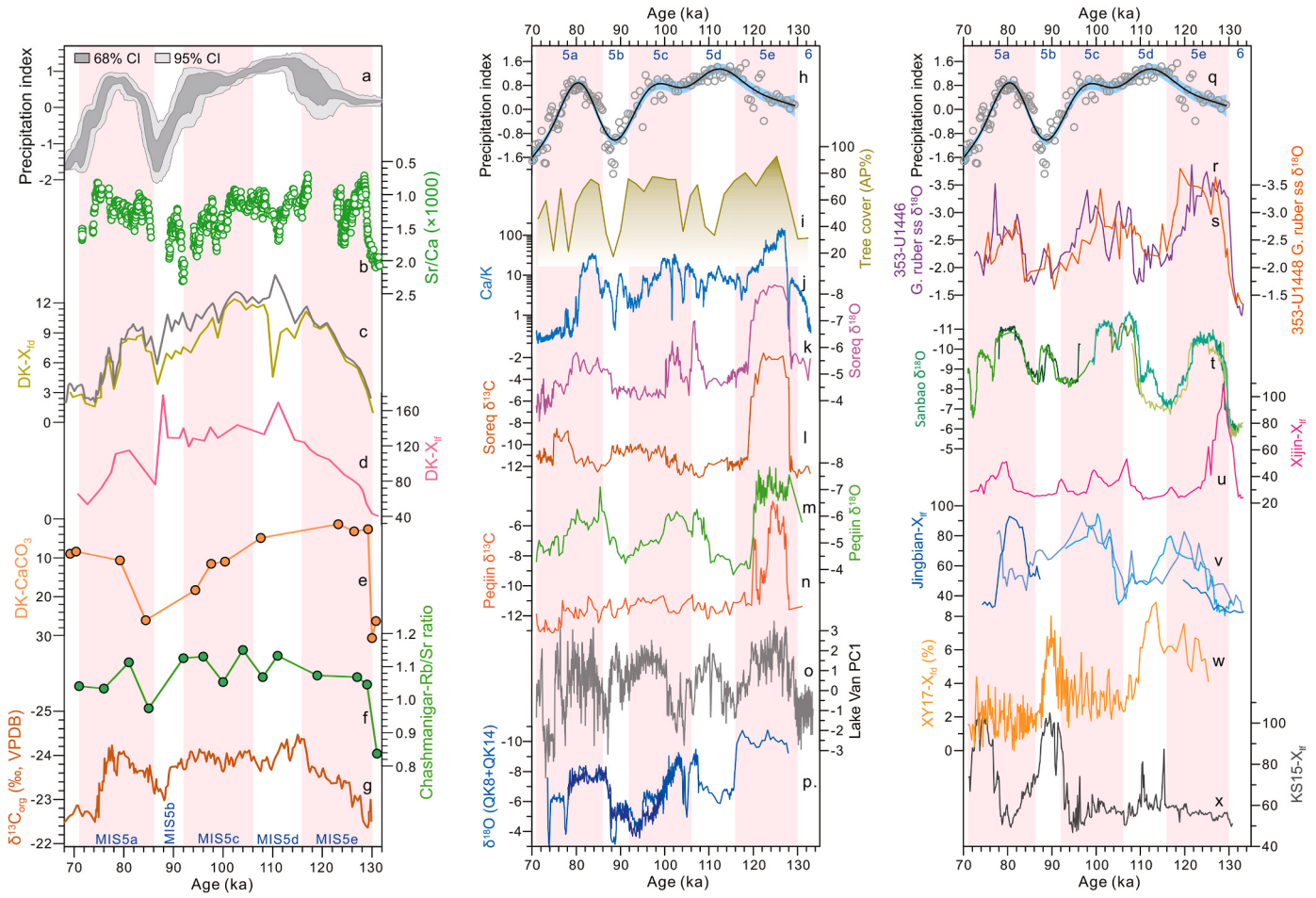


Fig. 4. Comparison of Marine Isotope Stage 5 precipitation from our study (a) to reference data for this time frame (b) the stalagmite Sr/Ca ratios from Tonnel'naya (Ton) cave, Uzbekistan, (c–e) frequency-dependent susceptibility (χ_{fd}), χ_{lf} , and CaCO_3 contents of Darai Kalon (DK) section (Häggi et al., 2019; Jia et al., 2018; Lu et al., 2020), (f) Rb/Sr ratios of Chashmanigar section (Yang et al., 2006), and (g) $\delta^{13}\text{C}_{\text{org}}$ record for the DK section (Wang et al., 2024). (a) refers to the probabilistic analysis results of the precipitation index. The gray line in (c) indicates χ_{fd} record of the DK section after carbonate correction (Wang et al., 2024). Comparisons of proxies show differences in precipitation patterns across Eurasia: (h, q) the precipitation index in this study [black line indicates generalized additive model (GAM) results; blue shading represents the 95 % confidence interval]; (i) pollen records at Lake Ohrid (Sadori et al., 2016); (j) Ca/K ratios of the 5045-1 core at Lake Ohrid (Francke et al., 2016); (k–n) oxygen and carbon stable isotope compositions of speleothems from Soreq and Peqiin caves (Bar-Matthews et al., 2003); (o) Lake Van Principal Component (PC) 1 hydroclimate record (Stockhecke et al., 2016); (p) oxygen stable isotope compositions of speleothems from QK cave in central NW Iran (Mehterian et al., 2017); (r, s) planktic foraminifera $\delta^{18}\text{O}$ compositions at Sites U1446 (northern Bay of Bengal) and U1448 (Andaman Sea) (Nilsson-Kerr et al., 2021); (t) speleothem $\delta^{18}\text{O}$ compositions of Sanbao cave from central China (Wang et al., 2008); (u) χ_{lf} changes of Xijin loess on the western Chinese Loess Plateau (Guo et al., 2022); (v) χ_{lf} changes of Jingbian loess at the East Asian desert margin (Stevens et al., 2018); (w) χ_{fd} changes in the XY17 loess from the Ili Basin (Li et al., 2020a); (x) χ_{lf} changes of KS15 loess (Li et al., 2018a). The 68 % (16th–84th percentile, dark gray) and 95 % (2.5th–97.5th percentile, light gray) confidence intervals (CIs) of the probability distributions are shown in (a). The pink shades mark the warm MIS 5a, c, e periods. (For interpretation of the references to color in this figure legend, the reader is referred to the Web version of this article.)

Although the highest ρ values are also observed in negative time displacements for CCM estimates between spring insolation gradient (IG) and precipitation, precipitation drives spring IG on a faster timescale, indicated by the relatively smaller optimum lag (Fig. 5k). Moreover, the significantly consistent variations in ρ with library sizes imply two-way interaction (Fig. 5k), which is unlikely. Hence, spring IG was not considered in the following discussions.

The above results of CCM analyses provide empirical evidence for pacemaker effects from orbital variations (obliquity and precession) and intrinsic mechanisms of the Earth system (including natural processes and feedback mechanisms that drive SST variability) on precipitation changes in southern CA. Reduced obliquity, which intensifies the equator-to-pole temperature gradient (Davis and Brewer, 2009; Routson et al., 2019), enhances westerlies and boost baroclinic potential energy (Davis and Brewer, 2009; Mantidis et al., 2011, 2014). This, in turn, strengthens storm systems and augment the frequency and intensity of cyclones and annual net precipitation at mid-latitudes (Chang et al.,

2002; Jackson and Broccoli, 2003; Molnar and England, 1990; Routson et al., 2019). Additionally, the amplified meridional temperature contrast drives the westerly jet southward (Zhou et al., 2020), directing the westerlies towards a more southerly trajectory over southern CA. Precession significantly influences the strength and latitudinal position of the westerlies (Li et al., 2020a; Yao et al., 2024; Zhong et al., 2025). Minimum precession (negative value) heightens seasonality and increases winter rainfall over CA (Häggi et al., 2019; Kutzbach et al., 2014; Li et al., 2013), due to the enhancement and southward shift of the winter rain storm track (Kutzbach et al., 2020). SST is a composite manifestation of multiple natural processes and feedback mechanisms within the Earth's climate system, including global ice volume, greenhouse gas concentration, ocean circulation, solar radiation forcing, and carbon cycling (Clark et al., 2024; Shakun et al., 2015; Snyder, 2016). These factors interact to shape the long-term trends and short-term variability of North Atlantic SST (Barker et al., 2011; Clark et al., 2024), which directly affects the moisture supply to CA. We thereby

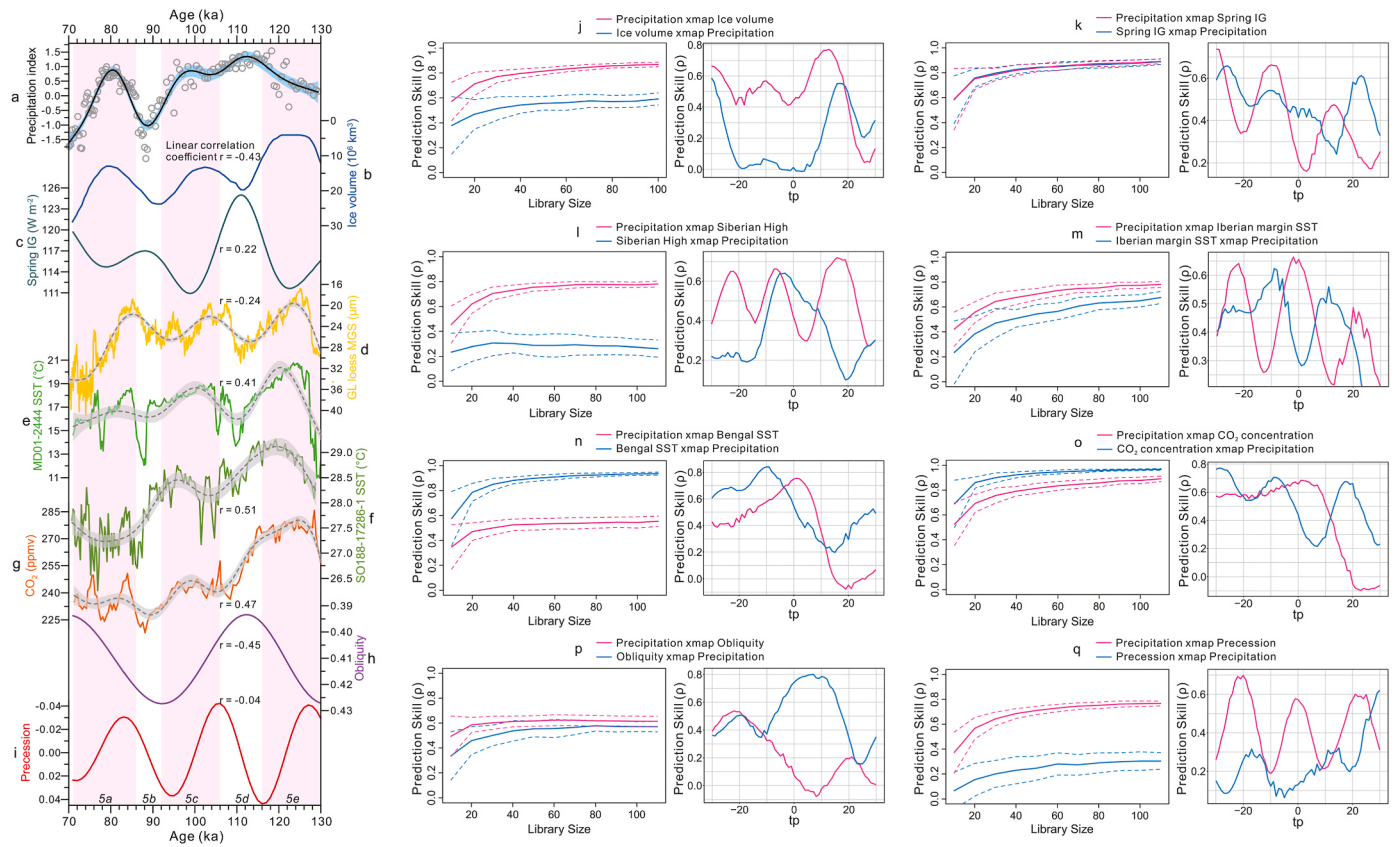


Fig. 5. Comparison between our GAM-smoothed precipitation index (a) and Northern Hemisphere ice volume (Ganopolski and Calov, 2011) (b); spring insolation gradient (IG) between 35°N and 55°N (Laskar et al., 2004) (c); Gulang (GL) loess mean grain size (MGS) (Sun et al., 2021) (d); sea surface temperature (SST) for MD01-2444 core on the Iberian Margin (Martrat et al., 2007) (e); SST for SO 188-17286-1 core from northern Bay of Bengal (Lauterbach et al., 2020) (f); CO₂ concentrations (Bereiter et al., 2012; Petit et al., 1999) (g); obliquity (Laskar et al., 2004) (h); and precession (Laskar et al., 2004) (i). Correlation of cross-mapped against observed values ("prediction skill (ρ)") as a function of the timeseries (library) length (size) (j–q). The "y xmap x" refers to prediction of variable x based on variable y, with higher ρ value indicating stronger causality. In time-delayed Convergent Cross-Mapping (CCM) analysis, negative (positive) time displacement of optimal ρ indicates genuine (no immediate) causal effect from x to y.

proposed a direct causal effect of North Atlantic (Iberian Margin) SST through moisture supply and indirect causal effects of orbital parameters by modulating intensity and position of the westerlies.

Based on the above discussions of precession, obliquity, and SST, we further explored the underlying driving mechanisms of MIS 5 precipitation patterns in southern CA. As marked by the blue and carmine dotted lines in Fig. 6a–d, SST in moisture source has a positive impact during MIS 5a–c; inversely, reduced obliquity coincides with increased precipitation during MIS 5d–e. Yet, minimum precession is not aligned with peak precipitation, hinting at their more complex causal associations. A near-antiphase lag and a ~90-degree phase lead of negative precession relative to the precipitation index in the precession band are observed during MIS 5d–e and MIS 5a–c, respectively (Fig. 6d). This demonstrates that precession forcing has not set the timing and strength of precipitation in southern CA during MIS 5d–e, while the precipitation index follows the negative precession with ~5 ka delay during MIS 5a–c. Given the phase lead/lag relationships, precession forcing more likely triggers precipitation changes in southern CA during MIS 5a–c. This is consistent with the precipitation response to SST, implying a potential connection between precession, SST, and precipitation in southern CA. Therefore, an alternative interpretation of precessional forcing might be that precession-driven variations in insolation have modulated the precipitation change in southern CA by influencing SST fluctuations.

These descriptions indicate the varying importance of precession, obliquity, and SST for regulating the MIS 5 precipitation pattern in southern CA. Focusing on the direct causal effect of moisture supply, we examined its monotonic relationship with the precipitation changes

using Spearman's rank correlation coefficient with a sliding window to precisely determine the timing of the transition between different climate dynamics. Overall, the coefficient rapidly increases and becomes positive since ca. 102 ka (Fig. 6e, pink stripe), which appears to be an important tipping point. North Atlantic SSTs become more dominant after ~102 ka, whereas obliquity has stronger impact prior to ~102 ka with a coefficient of −0.99. This most likely represents a transition of driving mechanisms, whereby westerly climate system controlled precipitation before ~102 ka, after which moisture supply became more decisive. Consequently, the contributions of westerlies change and moisture supply have changed over MIS 5, which has shaped the pattern of precipitation change in southern CA indicated by our results. Li et al. (2020a) indicated that moisture variability in the CA region on glacial-interglacial timescales was predominantly governed by changes in atmospheric humidity, which were modulated by the coupled variations of ice volume and greenhouse gases during glacial-interglacial cycles. Therefore, moisture availability was thought to be crucial for that transition throughout MIS 5, prompting a comparison of temperature-related boundary conditions – global ice volume and CO₂ concentration – with our results. As shown in Fig. 6f and g, mean sea level (representing global ice volume) and CO₂ concentration (yellow dotted lines) and their linear regression trends (gray dotted lines) intersect at ~102 ka. This suggests that higher temperatures prevailed prior to 102 ka, likely due to the lower ice-sheet albedo (reduced atmospheric cooling effect) and the enhanced warming effect of greenhouse gases. According to the Clausius–Clapeyron relation, these conditions have led to an increase in atmospheric water vapor (Held and

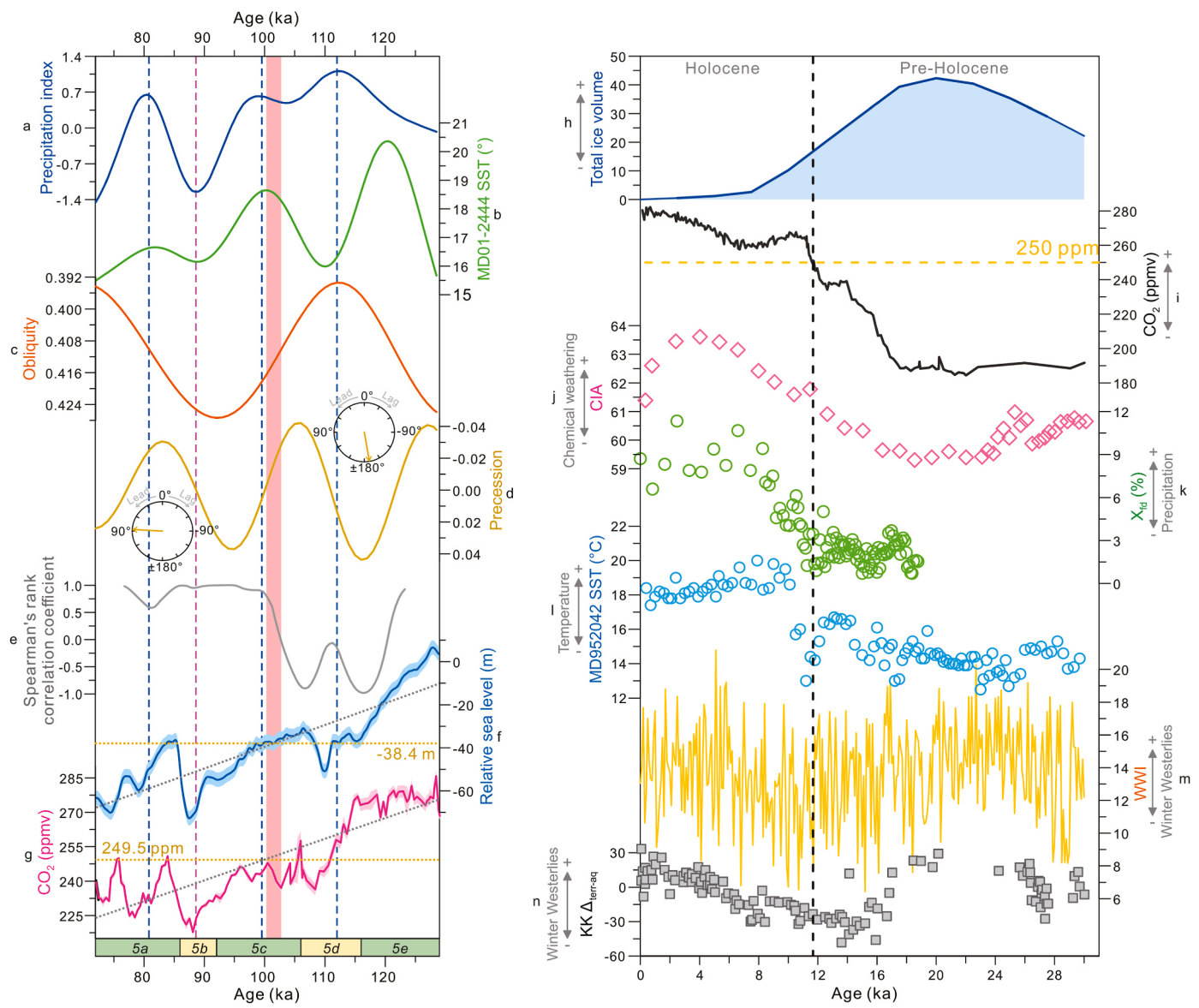


Fig. 6. Comparisons between the variations in precipitation index (a), Iberian Margin SST (b), obliquity (c), and precession (d), and relative sea level (Grant et al., 2012) (f) and CO₂ concentrations (g), during 76–124 ka. The phase wheels in (d) illustrating precipitation response in southern CA to (negative) precession before and after 102 ka. Positive/negative phases are measured in the anticlockwise/clockwise direction, representing phase lead/lag of negative precession relative to the precipitation index. (e) indicates Spearman correlation between precipitation index and Iberian Margin SST within a sliding window approach [window length = 20 (10 ka), step size = 1 (0.5 ka)]. In (f) and (g), the gray and yellow dotted lines indicate linear regression trends and means, respectively. Comparisons of the precipitation/humidity changes in Tajik Basin since ~30 ka indicated by the CIA values of a loess section located about 23 km to the south of Dushanbe (the capital of Tajikistan) (Tian et al., 2021) (j) and the χ_{fd} records of the KP loess section (Yang et al., 2020b) (k) with the total ice volume (10^6 kg^3) (Gowan et al., 2021) (h), the CO₂ concentrations (Bereiter et al., 2012; Petit et al., 1999) (i), the SST recorded by the cores MD952042 recovered on the Iberian Margin (Pailler and Bard, 2002) (l), and the intensity of the westerlies during winter (Aichner et al., 2019; Li et al., 2013) (m, n). (For interpretation of the references to color in this figure legend, the reader is referred to the Web version of this article.)

Soden, 2006; Li et al., 2020a; Miao et al., 2012), in contrast to the period following 102 ka. Simultaneously, decrease in global ice volume and increase in CO₂ concentration primarily contributed to increased SST (Clark et al., 2024). Consequently, overall higher global temperature and SST led to a rise in atmospheric humidity. In the context of sufficient atmospheric moisture prior to 102 ka, commonly higher precipitation was observed compared to that after 102 ka, and the precipitation changes in southern CA mainly followed the obliquity-driven westerly variations. As mentioned above, reduced obliquity strengthened the equator-to-pole temperature gradient, enhancing the westerlies and increasing atmospheric moisture delivery to CA (Davis and Brewer, 2009; Li et al., 2013; Routson et al., 2019). This amplified meridional temperature contrast also increased baroclinic potential energy, leading

to more frequent and intense cyclones and higher annual precipitation at mid-latitudes, including CA (Chang et al., 2002; Routson et al., 2019). Despite the distinctly different influence of obliquity on solar radiation observed between summer and winter, low obliquity reduced high-latitude summer insolation, leading to decreased ocean heat uptake, expanded sea ice, and year-round high-latitude cooling. This steepened the meridional temperature gradient and intensified the equatorward shift of the westerly jet (Lee and Poulsen, 2009; Lu et al., 2010; Timmermann et al., 2014; Zhong et al., 2024a).

By contrast, global cooling and ice sheet expansion have caused equatorial migration and intensification of the mid-latitude westerlies (Abell et al., 2021; Bridges et al., 2023; Sproson et al., 2024; Zhong et al., 2024b). In southern CA, therefore, moisture content was not constrained

by westerly transport, but rather by moisture supply from sources after 102 ka. In general, higher SSTs provide relatively more water vapor due to high evaporation rates over water vapor source regions (Li et al., 2020a), whereas lower SSTs can supply only a limited amount of water vapor, even with stronger westerlies. Thus, the precipitation index and the North Atlantic SST exhibited coincident variations after 102 ka (Fig. 6a and b). The variations in Mediterranean SST also displayed similarities with the orbital-scale North Atlantic SST changes during MIS 5 (Fig. S4a). Hence, the Iberian Margin SSTs are representative with respect to SSTs of oceanic moisture sources for CA precipitation in the aforementioned discussions.

The transition in precipitation drivers in southern CA identified here was also echoed by a similar, reversed, scenario subsequent to the Last Glacial Maximum. Prior to the Holocene, during a period of substantial ice sheet expansion and CO₂ concentrations remaining below 250 ppm (Fig. 6h and i), the changing trends of precipitation and atmospheric humidity in the study area were coeval with similar changes in Iberian Margin SST (Fig. 6j–l), contrary to the variations in winter westerly intensity (Fig. 6m–n). Comparisons of SST records suggested that the Iberian Margin SST was also representative of those of the oceanic moisture sources that contributed to precipitation in CA since 30 ka (Fig. S4b). During the Holocene with a dramatic decrease in ice volume and CO₂ concentrations above 250 ppm (Fig. 6h and i), the precipitation/humidity in the Tajik-Afghan depression changed in accordance with the increasingly intensified westerlies during the cold season, resulting in enhanced humidity during mid- and late-Holocene (Fig. 6j, k, m, n).

Collectively, our results revealed varying contributions of westerlies change and moisture supply to the MIS 5 precipitation changes in southern CA depending on boundary conditions. Although the transport of climatology water vapor in CA is dominated by mid-latitude westerlies, considering seasonality of precipitation as stated above, we argue that southern CA showed stronger sensitivity to moisture availability over MIS 5 than northern CA. The latter is primarily characterized by warm-season precipitation, with sufficient atmospheric moisture available during its main precipitation season. Hence, precipitation change was predominantly controlled by the strength of the westerlies in northern CA, with out of phase variation with those in Asian monsoon regions during MIS 5 (Li et al., 2020a) (Fig. 4w and x). In contrast, during cold seasons when water vapor evaporation rates are restricted in vapor source regions, the sensitivity of cold-season precipitation variations in southern CA to moisture supply may be amplified. Therefore, the sensitive response of precipitation to moisture supply and the transition in climate forcing dynamics during MIS 5 in southern CA were likely associated with the seasonality of precipitation.

Subsequently, we compared the MIS 5 precipitation change mechanisms in southern CA with those in the winter rainfall regions located to the west of our study area. In the Middle East and eastern Mediterranean, stalagmite and lake sediment records indicated that precession-induced maximum seasonality in boreal insolation caused the southward migration and strengthening of the westerlies during winter (Bar-Matthews et al., 2003; Mehterian et al., 2017; Stockhecke et al., 2016), which resulted in in-phase variations in the winter precipitation with Asian summer monsoon precipitation on the precessional scale (Fig. 4k–p, r–v). Nevertheless, the precession-related mechanism appeared to fall short of fully explaining the precipitation change patterns in southern CA, particularly for the period prior to 102 ka (Fig. 6a–d). Recently, an inverse association between the Holocene hydroclimatic changes in West Asia (WA) and spring insolation-driven shift of the subtropical high was documented and simulated (Chen et al., 2024; Ma et al., 2025). Despite being consistently dominated by cold-season westerly-driven precipitation, our results did not suggest that the MIS 5 precipitation changes in southern CA were broadly driven by the subtropical high controlled by spring insolation to the same degree as reported in WA (Fig. S4c–e). Since the westerlies-controlled regions are often assumed to have a consistent hydroclimate change

history, previous studies have integrated the hydroclimate variations of the Northern Hemisphere mid-latitudes (Routson et al., 2019). However, the above-mentioned comparisons emphasize significant regional differences in patterns of hydroclimate variation and their forcing mechanisms in the westerly-dominated mid-latitudes.

In addition, a CO₂ concentration of approximately 250 ppmv, which is typical for the boundary separating Quaternary glacial and interglacial periods, may, at least in part, if not entirely, induce a dynamic shift in the westerly-influenced climate at the onset of the Holocene and the termination of MIS 5e in southern CA (Fig. 6g–i). Parallels existed with easternmost Africa, where similar CO₂ level signaled a shift from energy-to moisture-limited climates at the onset of the Holocene (Baxter et al., 2023). This may suggest that CO₂ concentration plays a crucial role in modulating regional climate transitions as a critical threshold. However, the CO₂ threshold of 265 ppm was deemed essential for initiating the Oligocene-Miocene transition Glaciation (Greenop et al., 2019). The atmospheric CO₂ level of 260 ppm potentially represented an important threshold that influences ice-free conditions in the central Okhotsk Sea during MIS 5e and the early-mid Holocene (Lo et al., 2018). DeConto et al. (2008) even suggested a 280-pmm threshold for Northern Hemisphere glaciation during the Pliocene Epoch. Therefore, given the influence of ice volume on moisture supply, the precise CO₂ threshold for that transition in southern CA remains to be determined in the future.

3.5. Implications for early AMH dispersals across central Asia

The role of climate in AMH dispersal across Asia, and specifically the influence of major fluctuations in climate parameters such as moisture availability on AMH dispersal routes, so far remain poorly defined (Ao et al., 2024; Bae et al., 2017). AMH dispersal across the continent may be summarized as an earlier, low-density arrival during MIS 5 – a period by which Neanderthals and Denisovan populations were already established – followed by a rapid later dispersal during MIS4 and MIS3 which oversaw colonization of Australia and eventually Europe (Lamb et al., 2018). CA clearly plays a central role in the later, MIS3, major dispersal of AMH across Eurasia (Fitzsimmons et al., 2017; Zwyns et al., 2019), but there remains a lack of fossil and archaeological evidence for AMH in the region during MIS 5 (the first low-density migration wave, Fig. 7a and b) (Bae et al., 2017; Timmermann and Friedrich, 2016) and a dearth of paleoclimatic frameworks for the CA region which may explain this.

It is possible that AMH did not penetrate CA during MIS 5, since they were unable to effectively compete with existing populations of Denisovans and Neanderthals and were hindered by the relatively colder/drier climate conditions of the CA mountain corridor (Ao et al., 2024; Benazzi et al., 2011; Liu et al., 2015; Mellars, 2006; Zwyns et al., 2019). However, in CA, Neanderthals appeared relatively late (since MIS 5a) and the relevant fossil and archaeological sites are comparatively scarce (Asmerom et al., 2018; Bae et al., 2017). There is evidence for wetter conditions across CA during MIS 5 (Häggi et al., 2019; Li et al., 2020a; Lu et al., 2020; Yang et al., 2006); in southern CA, MIS 5 precipitation was quantified as exceeding 400 mm/a (Jia et al., 2018c), well above the 90 mm/a threshold required for hunter-gatherer survival (Beyer et al., 2021). Our paleo-precipitation reconstruction also indicates a persistent wetting trend from the onset of MIS 5, with high water vapor supply and precipitation levels maintained throughout MIS 5c–e (Fig. 2g–p, 3a, and 4a). Persistent wet conditions, occurring locally in the southern CA mountain corridor, potentially mitigate the proposal that precession-driven, high-frequency climatic fluctuations prevented human dispersals during this time (Schaebitz et al., 2021; Timmermann and Friedrich, 2016; Timmermann et al., 2022). Moreover, habitat suitability models yielded notably high likelihood of habitable conditions for AMH in CA at this time (Ao et al., 2024; Timmermann et al., 2022). We therefore argue that climatic conditions in southern CA may well have facilitated early AMH dispersal into the area during MIS 5.

The early MIS 5 AMH dispersal out of Africa was followed by a rapid dispersal during MIS4 and MIS3 along the southern Asian (summer

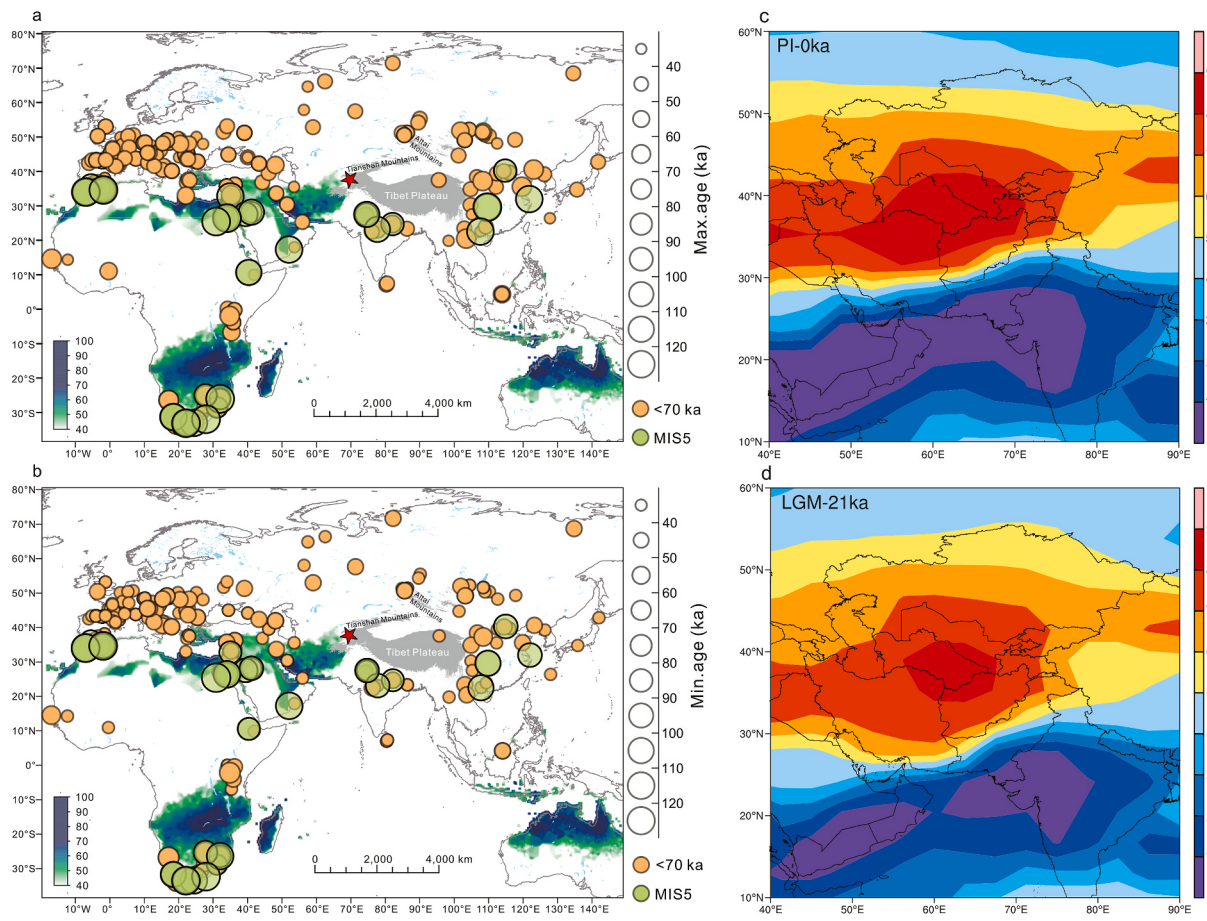


Fig. 7. Maps showing African–Eurasian *Homo sapiens* distributions since the last interglacial, drawn based on the single date, tier 1 category from Timmermann et al. (2022). In this category, only the core record is used, which excludes entries with uncertain species attributions, and multiple age estimates for a single archaeological layer are combined to provide a maximum (a) and minimum (b) age for the layer. The orange and green circles in the map are used to differentiate the archaeological layers between MIS 5 and the interval of 30–70 ka. The green shades indicate the percentage of winter (DJF) precipitation as a proportion of total annual precipitation (>50 %) for 1951–2000. The precipitation data source: the Global Precipitation Climatology Centre (GPCC) Climatology Version 2018 at 0.25° (Meyer-Christoffer et al., 2018). The red star marks the location of the CMG-B loess section. The proportion of the combined precipitation in both winter and spring to the total annual precipitation during pre-industrial (PI, c) period and the Last Glacial Maximum (LGM, d). The simulated data are extracted from the TraCE-21 ka dataset (Liu et al., 2009), which is output of the full TraCE simulation from 22,000 years before present (22ka) to 1990 CE. The simulation incorporates transient forcing changes in greenhouse gases, orbitally-driven insolation variations, ice sheets and meltwater fluxes. (For interpretation of the references to color in this figure legend, the reader is referred to the Web version of this article.)

monsoonal) coastal regions into southern China, with their eventual colonization of Australia (Bae et al., 2017; Liu et al., 2015; Timmermann and Friedrich, 2016). It appears that the archaeological sites, where *Homo sapiens* fossils were found during MIS 5, bypass the cold-season rainfall zones (Fig. 7). The uplift of the Tianshan Mountains commenced at 24–20 Ma (Hendrix et al., 1994; Yin et al., 1998), and may have accelerated since 11 Ma (Bullen et al., 2001; Chen et al., 2002; Heermance et al., 2007). The topographic evolutions have strongly affected the seasonality of precipitation in CA (Frisch et al., 2019; Rugenstein and Chamberlain, 2018; Sha et al., 2018). Fig. 7c, d shows the spatial distribution of precipitation seasonality independent of significant changes in climatic boundary conditions. Cold-season precipitation is dominant in Iran, Afghanistan, Turkmenistan, and Tajikistan. The southern periphery of Asia has favored warmer climates with summer rainfall peaks (Fig. 7c, d), and therefore we tentatively propose that the cold-season rainfall regime of southern CA may have prevented substantial AMH occupation in CA and further north during MIS 5. Lower temperatures in the cold seasons, despite higher precipitation, coupled with drier warm seasons, may have proved challenging for AMH arriving in the region during MIS 5. Temperature reductions will rapidly increase human mortality rates, particularly in resource-constrained seasons (Beyer et al., 2021; Timmermann and Friedrich, 2016;

Timmermann et al., 2022). Although we did note that similar conditions prevailed at this time in northeastern Africa and the Levant, where AMH clearly thrived (Fig. 7a and b), speleothem records and model simulations for MIS 5 suggested that summer monsoon penetrated northward into North Africa and provided reliable rainfall in the course of precession-driven high seasonality from 140 ka (Kutzbach et al., 2020; Orland et al., 2019). In this context, northeastern Africa and the Levant may still have provided favorable habitats, in stark contrast to the more continental CA with its limited access to summer monsoon rainfall (Chen et al., 2016; Häggi et al., 2019; Li et al., 2020a). This explanation may also have applied to last glacial age AMH dispersals (Fig. 7a and b). However, the distribution range of cold-season precipitation has reduced during the last glacial than pre-industrial period (Fig. 7c, d). Therefore, the reduction may increase AMH colonization probabilities in Southwest Asia (Fig. 7a and b).

4. Conclusions

In this paper, we undertook multi-proxy (grain size, χ_{lf} , color, TOC, and QCI) analyses of a loess section at Chashmanigar in southern Tajikistan to reconstruct orbital-scale precipitation variations during MIS 5 in southern CA. Given the fact that the variations in these proxies

are likely influenced by more than one factor, we employed PCA to assess their validity as a precipitation proxy, and subsequently developed a composite precipitation index. This index unveils a distinct precipitation pattern during MIS 5 that is characteristic of southern CA. Notably, the precipitation changes in southern CA during MIS 5 are markedly different from those observed in the Asian monsoon regions and the westerly-influenced Mediterranean, Middle East, and northern CA. Therefore, the precipitation drivers in southern CA cannot be fully attributed to the climatic mechanisms that dominate other regions.

We found a fundamental transition in precipitation dynamics in southern CA at ca. 102 ka, based on the reconstructed orbital-scale precipitation changes during MIS 5 in Tajikistan. Specifically, precipitation was dominated by the westerly climate subsystem prior to ca. 102 ka; after ca. 102 ka, it was primarily controlled by moisture supply from sources to the west. Temperature-driven availability of atmospheric moisture acted as the key determinant. Our analyses may inform future climate projections in southern CA, suggesting a continued wetting trend due to intensified greenhouse gas forcing and reduced obliquity, despite the impact of precession meriting further research. The reconstruction is also relevant for understanding AMH dispersal into Aisa. We argue that the ecosystems created by cold-season precipitation zone in southern CA may have impeded the dispersal of AMH northward into CA during MIS 5. Therefore, it is recommended that future habitat suitability models for estimating the probability of colonization by hominins should incorporate a closer scrutiny of the influence of precipitation seasonality in arid and semiarid regions.

Author contributions

Yue Li: Funding acquisition, Writing-Original Draft, Methodology, Conceptualization, Investigation, Formal Analysis, Visualization. Yougui Song: Resources, Funding acquisition, Writing-Review & Editing, Supervision, Formal Analysis, Validation. Kathryn E. Fitzsimmons: Formal analysis, Writing-Review & Editing, Validation. Aditi K. Dave: Formal analysis, Writing-Review & Editing, Validation. Junsheng Nie: Writing-Review & Editing, Validation. Christian Zeeden: Writing-Review & Editing, Validation. Shengli Yang: Data curation, Validation. Jovid Aminov: Investigation, Validation.

Declaration of competing interest

The authors declare that they have no known competing financial interests or personal relationships that could have appeared to influence the work reported in this paper.

Acknowledgements

We thank Dr. Xiaoxun Xie for his help in preparing Fig. 5. This work was financially supported by Natural Science Foundation of China (Grant No.: 42472254, 42372220), the Shaanxi Provincial Youth Science and Technology Nova Program (Grant No.: 2025ZC-KJXX-129), the Science and Technology Innovation Project of Laoshan Laboratory (Grant No.: LSKJ202203300), and the China Scholarship Council.

Appendix A. Supplementary data

Supplementary data to this article can be found online at <https://doi.org/10.1016/j.quascirev.2025.109594>.

Data availability

All data and/or code is contained within the submission.

References

- Abell, J.T., Winckler, G., Anderson, R.F., Herbert, T.D., 2021. Poleward and weakened westerlies during Pliocene warmth. *Nature* 589, 70–75. <https://doi.org/10.1038/s41586-01020-03062-41581>.
- Aichner, B., Makhmudov, Z., Rajabov, I., Zhang, Q., Pausata, F.S., Werner, M., Heinecke, L., Kuessner, M.L., Feakins, S.J., Sachse, D., 2019. Hydroclimate in the Pamirs was driven by changes in precipitation-evaporation seasonality since the last glacial period. *Geophys. Res. Lett.* 46, 13972–13983. <https://doi.org/10.11029/12019GL085202>.
- Ao, H., Ruan, J., Martín-Torres, M., Krapp, M., Liebrand, D., Dekkers, M.J., Caley, T., Jonell, T.N., Zhu, Z., Huang, C., 2024. Concurrent Asian monsoon strengthening and early modern human dispersal to East Asia during the last interglacial. *Proc. Natl. Acad. Sci.* 121, e2308994121.
- Asmerom, Y., Polyak, V.J., Wagner, J.D., Patchett, P.J., 2018. Hominin expansion into Central Asia during the last interglacial. *Earth Planet. Sci. Lett.* 494, 148–152. <https://doi.org/10.1016/j.epsl.2018.1004.1059>.
- Babesh, C., Achyuthan, H., Jaiswal, M.K., Lone, A., 2017. Late Quaternary loess-like paleosols and pedocomplexes, geochemistry, provenance and source area weathering, Manasbal, Kashmir Valley, India. *Geomorphology* 284, 191–205. <https://doi.org/10.1016/j.geomorph.2017.01.004>.
- Bae, C.J., Douka, K., Petraglia, M.D., 2017. On the origin of modern humans: Asian perspectives. *Science* 358, eaai9067. <https://doi.org/10.1126/science.aai9067>.
- Bar-Matthews, M., Ayalon, A., Gilmour, M., Matthews, A., Hawkesworth, C.J., 2003. Sea-land oxygen isotopic relationships from planktonic foraminifera and speleothems in the Eastern Mediterranean region and their implication for paleorainfall during interglacial intervals. *Geochim. Cosmochim. Acta* 67, 3181–3199. [https://doi.org/10.1016/S0016-7037\(02\)01031-1](https://doi.org/10.1016/S0016-7037(02)01031-1).
- Barker, S., Knorr, G., Edwards, R.L., Parrenin, F., Putnam, A.E., Skinner, L.C., Wolff, E., Ziegler, M., 2011. 800,000 years of abrupt climate variability. *Science* 334, 347–351. <https://doi.org/10.1126/science.120358>.
- Baxter, A., Verschuren, D., Peterse, F., Miralles, D., Martin-Jones, C., Maitiuertdi, A., Van der Meer, T., Van Daele, M., Lane, C., Haug, G., 2023. Reversed holocene temperature–moisture relationship in the Horn of Africa. *Nature* 620, 336–343. <https://doi.org/10.1038/s41586-023-06272-5>.
- Benazzi, S., Douka, K., Fornai, C., Bauer, C.C., Kullmer, O., Svoboda, J., Pap, I., Mallegni, F., Bayle, P., Coquerelle, M., 2011. Early dispersal of modern humans in Europe and implications for Neanderthal behaviour. *Nature* 479, 525–528.
- Bereiter, B., Lüthi, D., Siegrist, M., Schüpbach, S., Stocker, T.F., Fischer, H., 2012. Mode change of millennial CO₂ variability during the last glacial cycle associated with a bipolar marine carbon seesaw. *Proc. Natl. Acad. Sci.* 109, 9755–9760. <https://doi.org/10.1073/pnas.1204069109>.
- Beyer, R.M., Krapp, M., Eriksson, A., Manica, A., 2021. Climatic windows for human migration out of Africa in the past 300,000 years. *Nat. Commun.* 12, 4889. <https://doi.org/10.1038/s41467-021-24779-1>.
- Bisutti, I., Hilke, I., Raessler, M., 2004. Determination of total organic carbon – an overview of current methods. *TrAC-Trend Anal. Chem.* 23, 716–726. <https://doi.org/10.1016/j.trac.2004.09.003>.
- Blaauw, M., Christen, J.A., 2011. Flexible paleoclimate age-depth models using an autoregressive gamma process. *Bayesian Anal.* 6, 457–474. <https://doi.org/10.1214/1211-BA1618>.
- Blott, S.J., Pye, K., 2001. GRADISTAT: a grain size distribution and statistics package for the analysis of unconsolidated sediments. *Earth Surf. Process. Landf.* 26, 1237–1248. <https://doi.org/10.1002/esp.261>.
- Bridges, J.D., Tarduno, J.A., Cottrell, R.D., Herbert, T.D., 2023. Rapid strengthening of westerlies accompanied intensification of Northern Hemisphere glaciation. *Nat. Commun.* 14, 3905. <https://doi.org/10.1038/s41467-023-39557-4>.
- Bronger, A., Heinkele, T., 1990. Mineralogical and clay mineralogical aspects of loess research. *Quat. Int.* 7, 37–51. [https://doi.org/10.1016/1040-6182\(1090\)90037-90035](https://doi.org/10.1016/1040-6182(1090)90037-90035).
- Bullen, M., Burbank, D., Garver, J., Abdurakhmatov, K.Y., 2001. Late Cenozoic tectonic evolution of the northwestern Tien Shan: new age estimates for the initiation of mountain building. *Geol. Soc. Am. Bull.* 113, 1544–1559. [https://doi.org/10.1130/0016-7606\(2001\)113<1544:LCTEOT>2.0.CO;2](https://doi.org/10.1130/0016-7606(2001)113<1544:LCTEOT>2.0.CO;2).
- Buyałaert, J.-P., Challier, A., Kulakova, E., Taratunina, N., Thomsen, K., Utkina, A., Sosin, P., Tokareva, O., Anoikin, A., Khujageldiev, T., 2024. A luminescence dating study of the upper part of the loess-palaeosol sequence at kuldara, Khovaling Loess Plateau, Tajikistan. *Quat. Geochronol.* 82, 101545. <https://doi.org/10.1016/j.quageo.2024.101545>.
- Buyałaert, J.-P., Murray, A., Vandenberghe, D., Vriend, M., De Corte, F., 2008. Optical dating of Chinese loess using sand-sized quartz: establishing a time frame for Late Pleistocene climate changes in the western part of the Chinese Loess Plateau. *Quat. Geochronol.* 3, 99–113. <https://doi.org/10.1016/j.quageo.2007.05.003>.
- Buyałaert, J.-P., Jain, M., Murray, A.S., Thomsen, K.J., Thiel, C., Sohbati, R., 2012. A robust feldspar luminescence dating method for Middle and Late Pleistocene sediments. *Boreas* 41, 435–451. <https://doi.org/10.1111/j.1502-3885.2012.00248.x>.
- Cerling, T.E., Quade, J., Wang, Y., Bowman, J., 1989. Carbon isotopes in soils and palaeosols as ecology and palaeoecology indicators. *Nature* 341, 138–139. <https://doi.org/10.1038/341138a0>.
- Challier, A., Thomsen, K.J., Kurbanov, R., Sosin, P., Murray, A., Guérin, G., Meshcheryakova, O., Karayev, A., Khormali, F., Taratunina, N., Utkina, A., Buyałaert, J.-P., 2024. A detailed quartz and feldspar luminescence chronology for the Khorako II loess section (Southern Tajikistan). *Quat. Geochronol.* 83, 101571. <https://doi.org/10.1016/j.quageo.2024.101571>.

- Chang, E.K., Lee, S., Swanson, K.L., 2002. Storm track dynamics. *J. Clim.* 15, 2163–2183. [https://doi.org/10.1175/1520-0442\(2002\)2015<02163:STD>02162.02160.CO_02162](https://doi.org/10.1175/1520-0442(2002)2015<02163:STD>02162.02160.CO_02162).
- Chen, F., Chen, J., Huang, W., Chen, S., Huang, X., Jin, L., Jia, J., Zhang, X., An, C., Zhang, J., 2019. Westerlies Asia and monsoonal Asia: Spatiotemporal differences in climate change and possible mechanisms on decadal to sub-orbital timescales. *Earth Sci. Rev.* 192, 337–354. <https://doi.org/10.1016/j.earscirev.2019.03.005>.
- Chen, F.H., Jia, J., Chen, J.H., Li, G.Q., Zhang, X.J., Xie, H.C., Xia, D.S., Huang, W., An, C., B., 2016. A persistent Holocene wetting trend in arid central Asia, with wettest conditions in the late Holocene, revealed by multi-proxy analyses of loess-paleosol sequences in Xinjiang, China. *Quat. Sci. Rev.* 146, 134–146. <https://doi.org/10.1016/j.quascirev.2016.06.002>.
- Chen, J., Burbank, D., Schärer, K., Sobel, E., Yin, J., Rubin, C., Zhao, R., 2002. Magnetostratigraphy of the upper cenozoic strata in the southwestern Chinese tian Shan: rates of pleistocene folding and thrusting. *Earth Planet Sci. Lett.* 195, 113–130. [https://doi.org/10.1016/S0012-821X\(01\)00579-9](https://doi.org/10.1016/S0012-821X(01)00579-9).
- Chen, S., Chen, J., Ding, G., Ma, S., Ji, P., Zhou, A., Wu, D., Khormali, F., Hou, J., Chen, F., 2024. Dipole pattern of holocene hydroclimate variations across the Asian drylands: critical evidence from West Asia. *J. Geophys. Res. Atmos.* 129, e2023JD039413. <https://doi.org/10.1029/2023JD039413>.
- Chen, S., Chen, J., Lv, F., Liu, X., Huang, W., Wang, T., Liu, J., Hou, J., Chen, F., 2022. Holocene moisture variations in arid central Asia: Reassessment and reconciliation. *Quat. Sci. Rev.* 297, 107821. <https://doi.org/10.101016/j.quascirev.2022.107821>.
- Chen, T.H., Xie, Q.Q., Xu, H.F., Chen, J., Ji, J.F., Lu, H.Y., Balsam, W., 2010. Characteristics and formation mechanism of pedogenic hematite in Quaternary Chinese loess and paleosols. *Catena* 81, 217–225. <https://doi.org/10.1016/j.catena.2010.1004.1001>.
- Cheng, H., Spötl, C., Breitenbach, S.F., Sinha, A., Wassenburg, J.A., Jochum, K.P., Scholz, D., Li, X., Yi, L., Peng, Y., 2016. Climate variations of Central Asia on orbital to millennial timescales. *Sci. Rep.* 6, 36975. <https://doi.org/10.1038/srep36975>.
- Clark, A.T., Ye, H., Isbell, F., Deyle, E.R., Cowles, J., Tilman, G.D., Sugihara, G., 2015. Spatial convergent cross mapping to detect causal relationships from short time series. *Ecology* 96, 1174–1181. <https://doi.org/10.1890/14-1479.1>.
- Clark, P.U., Shakun, J.D., Rosenthal, Y., Köhler, P., Bartlein, P.J., 2024. Global and regional temperature change over the past 4.5 million years. *Science* 383, 884–890. <https://doi.org/10.1126/science.ad1908>.
- Davis, B.A.S., Brewer, S., 2009. Orbital forcing and role of the latitudinal insolation/temperature gradient. *Clim. Dyn.* 32, 143–165. <https://doi.org/10.1007/s00382-008-0480-9>.
- Dearing, J., 1999. Magnetic Susceptibility, Environmental Magnetism: A Practical Guide, pp. 35–62. <https://cir.nii.ac.jp/crid/1572261550466866560>.
- DeConto, R.M., Pollard, D., Wilson, P.A., Pälike, H., Lear, C.H., Pagani, M., 2008. Thresholds for Cenozoic bipolar glaciation. *Nature* 455, 652–656. <https://doi.org/10.1038/nature07337>.
- Demeter, F., Shackelford, L.L., Bacon, A.-M., Düringer, P., Westaway, K., Sayavongkhambay, T., Braga, J., Sichanthonthip, P., Khamdalavong, P., Ponche, J.-L., 2012. Anatomically modern human in Southeast Asia (Laos) by 46 ka. *Proc. Natl. Acad. Sci.* 109, 14375–14380. <https://doi.org/10.1073/pnas.1208104109>.
- Deyle, E.R., Sugihara, G., 2011. Generalized theorems for nonlinear state space reconstruction. *PLoS One* 6, e18295. <https://doi.org/10.1371/journal.pone.0018295>.
- Dima, M., Nicita, D.R., Lohmann, G., Ionita, M., Voiculescu, M., 2021. Early-onset of Atlantic meridional overturning circulation weakening in response to atmospheric CO₂ concentration. *npj Clim. Atmos. Sci.* 4, 27. <https://doi.org/10.1038/s41612-41021-00182-x>.
- Ding, Z.L., Ranov, V., Yang, S.J., Finaev, A., Han, J.M., Wang, G.A., 2002. The loess record in southern Tajikistan and correlation with Chinese loess. *Earth Planet Sci. Lett.* 200, 387–400. [https://doi.org/10.1016/S0012-821X\(02\)00637-4](https://doi.org/10.1016/S0012-821X(02)00637-4).
- Dodonov, A., Sadchikova, T., Sedov, S., Simakova, A., Zhou, L., 2006. Multidisciplinary approach for paleoenvironmental reconstruction in loess-paleosol studies of the Darai Kalon section, Southern Tajikistan. *Quat. Int.* 152, 48–58. <https://doi.org/10.1016/j.quaint.2005.1012.1001>.
- Dodonov, A.E., Baiguzina, L.L., 1995. Loess stratigraphy of central Asia: palaeoclimatic and palaeoenvironmental aspects. *Quat. Sci. Rev.* 14, 707–720. [https://doi.org/10.1016/0277-3791\(95\)00054-2](https://doi.org/10.1016/0277-3791(95)00054-2).
- Duller, G.A.T., 2015. The Analyst software package for luminescence data: overview and recent improvements. *Ancient TL* 33, 35–42. <https://www.ancienttl.org/article/download/6753/5863>.
- Fan, Y., Jia, J., Xia, D., Meadows, M., Wang, Z., 2021. Seasonality of response to millennial-scale climate events of the last glacial: evidence from loess records over mid-latitude Asia. *Geochem. Geophys. Geosyst.* 22, e2021GC009903.
- Fang, C., Smith, P., Moncrieff, J., Smith, J.U., 2005. Similar response of labile and resistant soil organic matter pools to changes in temperature. *Nature* 433, 57–59. <https://doi.org/10.1038/nature03138>.
- Fischer, H., Meissner, K.J., Mix, A.C., Abram, N.J., Auer, J., Brovkin, V., Capron, E., Colombaroli, D., Daniau, A.-L., Dyez, K.A., 2018. Palaeoclimate constraints on the impact of 2 °C anthropogenic warming and beyond. *Nat. Geosci.* 11, 474–485. <https://doi.org/10.1038/s41561-018-0146-0>.
- Fitzsimmons, K.E., Iovita, R., Sprafke, T., Glantz, M., Talamo, S., Horton, K., Beeton, T., Alipova, S., Bekseitov, G., Ospanov, Y., 2017. A chronological framework connecting the early Upper Palaeolithic across the Central Asian piedmont. *J. Hum. Evol.* 113, 107–126. <https://doi.org/10.1016/j.jhevol.2017.07.006>.
- Forster, T., Heller, F., 1994. Loess deposits from the Tajik depression (Central-Asia) - magnetic-properties and paleoclimate. *Earth Planet Sci. Lett.* 128, 501–512. [https://doi.org/10.1016/0012-821X\(1094\)90166-X](https://doi.org/10.1016/0012-821X(1094)90166-X).
- Francke, A., Wagner, B., Just, J., Leicher, N., Gromig, R., Baumgarten, H., Vogel, H., Lacey, J.H., Sadori, L., Wonik, T., 2016. Sedimentological processes and environmental variability at Lake Ohrid (Macedonia, Albania) between 637 ka and the present. *Biogeosciences* 13, 1179–1196. <https://doi.org/10.5194/bg-1113-1179-2016>.
- Frechen, M., Dodonov, A.E., 1998. Loess chronology of the Middle and upper pleistocene in Tadzhikistan. *Geol. Rundsch.* 87, 2–20. <https://doi.org/10.1007/s005310050185>.
- Frisch, K., Voigt, S., Verestek, V., Appel, E., Albert, R., Gerdes, A., Arndt, I., Raddatz, J., Voigt, T., Weber, Y., 2019. Long-period astronomical forcing of westerlies' strength in Central Asia during Miocene climate cooling. *Paleoceanogr. Paleoclimatol.* 34, 1784–1806. <https://doi.org/10.1029/2019PA003642>.
- Galbraith, R.F., Roberts, R.G., Laslett, G.M., Yoshida, H., Olley, J.M., 1999. Optical dating of single and multiple grains of quartz from Jinmium rock shelter, northern Australia: Part I, experimental design and statistical models. *Archaeometry* 41, 339–364. <https://doi.org/10.1111/j.1475-4754.1999.tb00987.x>.
- Ganopolski, A., Calov, R., 2011. The role of orbital forcing, carbon dioxide and regolith in 100 kyr glacial cycles. *Clim. Past* 7, 1415–1425. <https://doi.org/10.5194/cp-1417-1415-2011>.
- Gao, F., Jia, J., Xia, D., Lu, C., Lu, H., Wang, Y., Liu, H., Ma, Y., Li, K., 2019. Asynchronous Holocene climate optimum across mid-latitude Asia. *Palaeoclim. Palaeoecol.* 518, 206–214. <https://doi.org/10.1016/j.palaeo.2019.01.012>.
- Gao, F., Yang, J., Wang, S., Wang, Y., Li, K., Wang, F., Ling, Z., Xia, D., 2022. Variation of the winter mid-latitude Westerlies in the Northern Hemisphere during the Holocene revealed by aeolian deposits in the southern Tibetan Plateau. *Quat. Res.* 107, 104–112. <https://doi.org/10.1017/qj.qua.2021.1065>.
- Gao, X., Hao, Q., Wang, L., Song, Y., Ge, J., Wu, H., Xu, B., Han, L., Fu, Y., Wu, X., 2024. Changes in monsoon precipitation in East Asia under a 2 °C interglacial warming. *Sci. Adv.* 10, eadm7694. <https://www.science.org/doi/7610.1126/sciadv.adm7694>.
- Gao, X.B., Hao, Q.Z., Wang, L., Oldfield, F., Bloemendal, J., Deng, C.L., Song, Y., Ge, J.Y., Wu, H.B., Xu, B., Li, F.J., Han, L., Fu, Y., Guo, Z.T., 2018. The different climatic response of pedogenic hematite and ferrimagnetic minerals: evidence from particle-sized modern soils over the Chinese Loess Plateau. *Quat. Sci. Rev.* 179, 69–86. <https://doi.org/10.1016/j.quascirev.2017.1011.1011>.
- Glantz, M., Van Arsdale, A., Temirbekov, S., Beeton, T., 2018. How to survive the glacial apocalypse: hominin mobility strategies in late Pleistocene Central Asia. *Quat. Int.* 466, 82–92. <https://doi.org/10.1016/j.quaint.2016.06.037>.
- Gowan, E.J., Zhang, X., Khosravi, S., Rovere, A., Stocchi, P., Hughes, A.L., Gyllencreutz, R., Mangerud, J., Svendsen, J.I., Lohmann, G., 2021. A new global ice sheet reconstruction for the past 80 000 years. *Nat. Commun.* 12, 1199. <https://doi.org/10.1038/s41467-41021-21469-w>.
- Grant, K., Rohling, E., Bar-Matthews, M., Ayalon, A., Medina-Elizalde, M., Ramsey, C.B., Satow, C., Roberts, A., 2012. Rapid coupling between ice volume and polar temperature over the past 150,000 years. *Nature* 491, 744–747. <https://doi.org/10.1038/nature11593>.
- Greenop, R., Sodisan, S.M., Henehan, M.J., Wilson, P.A., Lear, C.H., Foster, G.L., 2019. Orbital forcing, ice volume, and CO₂ across the Oligocene-Miocene transition. *Paleoceanogr. Paleoclimatol.* 34, 316–328. <https://doi.org/10.1029/2018PA003420>.
- Grehan, G., Gouesbet, G., 1979. Mie theory calculations - new progress, with emphasis on particle sizing. *Appl. Opt.* 18, 3489–3493. <https://doi.org/10.1364/AO.18.003489>.
- Gu, F., Wu, G., Zhang, C., Yan, N., Huang, J., 2020. Geochemistry of surface soil in the Eastern Pamirs and its implications for Muqttagata ice core dust provenance. *Appl. Geochem.* 121, 104724. <https://doi.org/10.101016/j.apgeochem.102020.104724>.
- Guérin, G., Mercier, N., Adamiec, G., 2011. Dose-rate conversion factors: update. *Ancient TL* 29, 5–8. <http://www.aber.ac.uk/ancient-tl>.
- Guo, B., Nie, J., Stevens, T., Buylaert, J.-P., Peng, T., Xiao, W., Pan, B., Fang, X., 2022. Dominant precessional forcing of the East Asian summer monsoon since 260 ka. *Geology* 50, 1372–1376. <https://doi.org/10.1130/G50206.50201>.
- Guo, Z.T., Berger, A., Yin, Q.Z., Qin, L., 2009. Strong asymmetry of hemispheric climates during MIS-13 inferred from correlating China loess and Antarctica ice records. *Clim. Past* 5, 21–31. <https://doi.org/10.5194/cp-5195-5121-2009>.
- Häggé, C., Eglington, T.I., Zech, W., Sosin, P., Zech, R., 2019. A 250 ka leaf-wax δD record from a loess section in Darai Kalon, Southern Tajikistan. *Quat. Sci. Rev.* 208, 118–128. <https://doi.org/10.1016/j.quascirev.2019.1001.1019>.
- Hastie, T., Tibshirani, R., 1986. Generalized additive models. *Stat. Sci.* 1, 297–310. <https://doi.org/10.1214/ss/1177013604>.
- Heermance, R.V., Chen, J., Burbank, D.W., Wang, C., 2007. Chronology and tectonic controls of Late Tertiary deposition in the southwestern Tian Shan foreland, NW China. *Basin Res.* 19, 599–632. <https://doi.org/10.1111/j.1365-2117.2007.00339.x>.
- Held, I.M., Soden, B.J., 2006. Robust responses of the hydrological cycle to global warming. *J. Clim.* 19, 5686–5699. <https://doi.org/10.1175/JCLI3990.1>.
- Hendrix, M.S., Dumitru, T.A., Graham, S.A., 1994. Late Oligocene-early Miocene unroofing in the Chinese Tian Shan: an early effect of the India-Asia collision. *Geology* 22, 487–490. [https://doi.org/10.1130/0091-7613\(1994\)022<487:LOEUMI>2.3.CO;2](https://doi.org/10.1130/0091-7613(1994)022<487:LOEUMI>2.3.CO;2).
- Hobart, B., Lisiecki, L.E., Rand, D., Lee, T., Lawrence, C.E., 2023. Late Pleistocene 100-kyr glacial cycles paced by precession forcing of summer insolation. *Nat. Geosci.* 16, 717–722. <https://doi.org/10.1038/s41561-41023-01235-x>.
- Hu, H.-M., Marino, G., Pérez-Mejías, C., Spötl, C., Yokoyama, Y., Yu, J., Rohling, E., Kano, A., Ludwig, P., Pinto, J.G., 2024. Sustained North Atlantic warming drove anomalously intense MIS 11c interglacial. *Nat. Commun.* 15, 5933. <https://doi.org/10.1038/s41467-024-50207-1>.
- Huang, J., Yu, H., Guan, X., Wang, G., Guo, R., 2016. Accelerated dryland expansion under climate change. *Nat. Clim. Change* 6, 166–171. <https://doi.org/10.1038/nclimate2837>.

- Huntley, D.J., Baril, M., 1997. The K content of the K-feldspars being measured in optical dating or in thermoluminescence dating. *Ancient TL* 15, 11–13. <https://www.sfu.ca/physics/huntley/83paper.pdf>.
- Huntley, D.J., Hancock, R., Ancient, T., 2001. The Rb contents of the K-feldspar grains being measured in optical dating. *Ancient TL* 19, 43–46. <https://www.sfu.ca/physics/research/workarea/huntley/98paper.pdf>.
- Jackson, C., Broccoli, A., 2003. Orbital forcing of Arctic climate: mechanisms of climate response and implications for continental glaciation. *Clim. Dyn.* 21, 539–557. <https://doi.org/10.1007/s00382-00003-00351-00383>.
- Ji, J.F., Balsam, W., Chen, J., 2001. Mineralogic and climatic interpretations of the Luochuan loess section (China) based on diffuse reflectance spectrophotometry. *Quat. Res.* 56, 23–30. <https://doi.org/10.1006/qres.2001.2238>.
- Ji, J.F., Chen, J., Balsam, W., Lu, H.Y., Sun, Y.B., Xu, H.F., 2004. High resolution hematite/goethite records from Chinese loess sequences for the last glacial-interglacial cycle: rapid climatic response of the East Asian Monsoon to the tropical Pacific. *Geophys. Res. Lett.* 31. <https://doi.org/10.1029/2003GL018975>.
- Jia, J., Fuyuan, G., Dunsheng, X., Wei, H., Fahu, C., 2018a. Moisture variations in arid central Asia and its out-of-phase relationship with the Asian Monsoon during MIS 5: evidence from loess records. *J. Quat. Sci.* 33, 435–443. <https://doi.org/10.1002/jqs.3024>.
- Jia, J., Liu, H., Gao, F., Xia, D., 2018b. Variations in the westerlies in central Asia since 16ka recorded by a loess section from the tien Shan mountains. *Palaeogeogr. Palaeoclimatol. Palaeoecol.* 504, 156–161. <https://doi.org/10.1016/j.palaeo.2018.1005.1021>.
- Jia, J., Liu, H., Wang, Y., Xia, D., 2018c. Variations in the iron mineralogy of a loess section in Tajikistan during the Mid-Pleistocene and Late Pleistocene: implications for the climatic evolution in central Asia. *Geochem. Geophys. Geosyst.* 19, 1244–1258. <https://doi.org/10.1002/2017GC007371>.
- Jia, R., Lin, B., 1993. Preliminary research on lipids in loess and paleosol of Duanjiapo section near Xi'an. *Sci. Geogr. Sin.* 13, 338–345, 310.13249/j.cnki.sgs.11993.13204.13337 (in Chinese with English abstract).
- Jiang, J., Zhou, T., Chen, X., Zhang, L., 2020. Future changes in precipitation over Central Asia based on CMIP6 projections. *Environ. Res. Lett.* 15, 054009, 054010.051088/051748-059326/ab054007d054003.
- Jiang, J., Zhou, T.J., 2021. Human-induced rainfall reduction in drought-prone northern central Asia. *Geophys. Res. Lett.* 48, e2020GL092156. <https://doi.org/10.10910/092020GL092156>.
- Jiang, Z., Liu, Q., Roberts, A.P., Dekkers, M.J., Barrón, V., Torrent, J., Li, S., 2022. The magnetic and color reflectance properties of hematite: from Earth to Mars. *Rev. Geophys.* 60, e2020RG000698. <https://doi.org/10.1029/2020RG000698>.
- Jolliffe, I.T., Cadima, J., 2016. Principal component analysis: a review and recent developments. *Philos. T. R. Soc. A* 374, 20150202. <https://doi.org/10.1098/rsta.2015.0202>.
- Kang, J., Zan, J., Bai, Y., Fang, X., Chen, C., Guan, C., Khodzhiev, A., 2020. Critical altitudinal shift from detrital to pedogenic origin of the magnetic properties of surface soils in the western Pamir Plateau, Tajikistan. *Geochem. Geophys. Geosyst.* 21, e2019GC008752. <https://doi.org/10.001029/002019GC008752>.
- Kassambara, A., Mundt, F., 2017. Package ‘factoextra’. Extract and visualize the results of multivariate data analyses 76. <http://www.sthda.com/english/rpkgs/factoextra>.
- Knorr, W., Prentice, I.C., House, J.I., Holland, E.A., 2005. Long-term sensitivity of soil carbon turnover to warming. *Nature* 433, 298–301. <https://doi.org/10.1038/nature03226>.
- Kong, X., Zhou, W., Beck, J.W., Xian, F., Qiang, X., Ao, H., Wu, Z., An, Z., 2020. Loess magnetic susceptibility flux: a new proxy of East Asian monsoon precipitation. *J. Asian Earth Sci.* 201, 104489. <https://doi.org/10.101016/j.jseas.2020.104489>.
- Koutsodendris, A., Dakos, V., Fletcher, W.J., Knipping, M., Kotthoff, U., Milner, A.M., Müller, U.C., Kaboth-Bahr, S., Kern, O.A., Kolb, L., 2023. Atmospheric CO₂ forcing on Mediterranean biome dynamics during the past 500 kyr. *Nat. Commun.* 14, 1664. <https://doi.org/10.1038/s41467-41023-37388-x>.
- Kutzbach, J., Chen, G., Cheng, H., Edwards, R., Liu, Z., 2014. Potential role of winter rainfall in explaining increased moisture in the Mediterranean and Middle East during periods of maximum orbitally-forced insolation seasonality. *Clim. Dyn.* 42, 1079–1095. <https://doi.org/10.1007/s00382-0013-01692-00381>.
- Kutzbach, J.E., Guan, J., He, F., Cohen, A.S., Orland, I.J., Chen, G., 2020. African climate response to orbital and glacial forcing in 140,000-y simulation with implications for early modern human environments. *Proc. Natl. Acad. Sci.* 117, 2255–2264. <https://doi.org/10.1073/pnas.1917673117>.
- Lamb, H.F., Bates, C.R., Bryant, C.L., Davies, S.J., Huws, D.G., Marshall, M.H., Roberts, H.M., Toland, H., 2018. 150,000-year palaeoclimate record from northern Ethiopia supports early, multiple dispersals of modern humans from Africa. *Sci. Rep.* 8, 1077. <https://doi.org/10.1038/s41598-018-19601-w>.
- Laskar, J., Robutel, P., Joutel, F., Gastineau, M., Correia, A.C.M., Levrard, B., 2004. A long-term numerical solution for the insolation quantities of the Earth. *Astron. Astrophys.* 428, 261–285. <https://doi.org/10.1051/0004-6361:20041335>.
- Lauterbach, S., Andersen, N., Wang, Y.V., Blanz, T., Larsen, T., Schneider, R.R., 2020. Añ 130 kyr record of surface water temperature and δ₁₈O from the northern Bay of Bengal: Investigating the linkage between Heinrich events and weak monsoon intervals in Asia. *Paleoceanogr. Paleoclimatol.* 35, e2019PA003646. <https://doi.org/10.001029/002019PA003646>.
- Lê, S., Josse, J., Husson, F., 2008. FactoMineR: an R package for multivariate analysis. *J. Stat. Softw.* 25, 1–18. <https://doi.org/10.18637/jss.v18025.i18601>.
- Lee, S.-Y., Poulsen, C.J., 2009. Obliquity and precessional forcing of continental snow fall and melt: implications for orbital forcing of Pleistocene ice ages. *Quat. Sci. Rev.* 28, 2663–2674. <https://doi.org/10.1016/j.quascirev.2009.06.002>.
- Li, B., Li, S., 2012. A reply to the comments by Thomsen et al. on “Luminescence dating of K-feldspar from sediments: A protocol without anomalous fading correction”. *Quat. Geochronol.* 8, 49–51. <https://doi.org/10.1016/j.quageo.2011.10.001>.
- Li, C., Zhang, C., Luo, G., Chen, X., Maisupova, B., Madaminov, A.A., Han, Q., Djebbaev, B.M., 2015. Carbon stock and its responses to climate change in Central Asia. *Glob. Change Biol.* 21, 1951–1967. <https://doi.org/10.1111/gcb.12846>.
- Li, G., Chen, F., Xia, D., Yang, H., Zhang, X., Madsen, D., Oldknow, C., Wei, H., Rao, Z., Qiang, M., 2018a. A Tianshan Mountains loess-paleosol sequence indicates anti-phase climatic variations in arid central Asia and in East Asia. *Earth Planet Sci. Lett.* 494, 153–163. <https://doi.org/10.1016/j.epsl.2018.1004.1052>.
- Li, G., Yang, H., Stevens, T., Zhang, X., Zhang, H., Wei, H., Zheng, W., Li, L., Liu, X., Chen, J., 2020a. Differential ice volume and orbital modulation of Quaternary moisture patterns between Central and East Asia. *Earth Planet Sci. Lett.* 530, 115901. <https://doi.org/10.11016/j.epsl.112019.115901>.
- Li, M., Hinno, L., Kump, L., 2019a. Acycle: time-series analysis software for paleoclimate research and education. *Comput. Geosci.* 127, 12–22. <https://doi.org/10.1016/j.cageo.2019.1002.1011>.
- Li, X., Liu, X., Qiu, L., An, Z., Yin, Z.Y., 2013. Transient simulation of orbital-scale precipitation variation in monsoonal East Asia and arid central Asia during the last 150 ka. *J. Geophys. Res. Atmos.* 118, 7481–7488. <https://doi.org/10.1002/jgrd.50611>.
- Li, Y., Song, Y., Chen, X., Li, J., Mamadjanov, Y., Aminov, J., 2016. Geochemical composition of Tajikistan loess and its provenance implications. *Palaeogeogr. Palaeoclimatol. Palaeoecol.* 446, 186–194. <https://doi.org/10.1016/j.palaeo.2016.01.025>.
- Li, Y., Song, Y., Fitzsimmons, K.E., Dave, A.K., Liu, Y., Zong, X., Sun, H., Liu, H., Orozbaev, R., 2022. Investigating potential links between fine-grained components in loess and westerly airflow: evidence from East and central Asia. *Front. Earth Sci.* 10, 901629. <https://doi.org/10.90339/feart.902022.901629>.
- Li, Y., Song, Y., Kaskaoutis, D.G., Chen, X., Mamadjanov, Y., Tan, L., 2019b. Atmospheric dust dynamics in southern Central Asia: implications for buildup of Tajikistan loess sediments. *Atmos. Res.* 229, 74–85. <https://doi.org/10.1016/j.atmosres.2019.1006.1013>.
- Li, Y., Song, Y., Li, X., Xie, X., Kaskaoutis, D.G., Aminov, J., Yatimov, S., 2024. Aeolian dust dynamics in southern Central Asia revealed by the multi-timescale loess records in southern Tajikistan. *Geomorphology* 467, 109461. <https://doi.org/10.101016/j.geomorph.102024.109461>.
- Li, Y., Song, Y., Orozbaev, R., Dong, J., Li, X., Zhou, J., 2020b. Moisture evolution in central Asia since 26 ka: insights from a Kyrgyz loess section, western tian Shan. *Quat. Sci. Rev.* 249, 106604. <https://doi.org/10.101016/j.quascirev.2020.106604>.
- Li, Z.J., Wang, F., Wang, X., Li, B.F., Chen, F.H., 2018b. A multi-proxy climatic record from the central Tengger Desert, southern Mongolian Plateau: implications for the aridification of inner Asia since the late Pliocene. *J. Asian Earth Sci.* 160, 27–37. <https://doi.org/10.1016/j.jseas.2018.1003.1022>.
- Liang, P., Forman, S.L., 2019. LDAC: an Excel-based program for luminescence equivalent dose and burial age calculations. *Ancient TL* 37, 21–40. <https://doi.org/10.26034/la.atl.2201.26536>.
- Lin, Y.C., Mu, G.J., Xu, L.S., Zhao, X., 2016. The origin of bimodal grain-size distribution for aeolian deposits. *Aeolian Res* 20, 80–88. <https://doi.org/10.1016/j.aeolia.2015.1012.1001>.
- Liou, Q.S., Roberts, A.P., Larrasoana, J.C., Banerjee, S.K., Guyodo, Y., Tauxe, L., Oldfield, F., 2012. Environmental magnetism: Principles and applications. *Rev. Geophys.* 50. <https://doi.org/10.1029/2012RG000393>.
- Liu, W., Jin, C.Z., Zhang, Y.-Q., Cai, Y.-J., Xing, S., Wu, X.-J., Cheng, H., Edwards, R.L., Pan, W.-S., Qin, D.-G., 2010. Human remains from Zhirendong, south China, and modern human emergence in East Asia. *Proc. Natl. Acad. Sci.* 107, 19201–19206. <https://doi.org/10.1073/pnas.1014386107>.
- Liu, W., Martinón-Torres, M., Cai, Y.-J., Xing, S., Tong, H.-W., Pei, S.-W., Sier, M.J., Wu, X.-H., Edwards, R.L., Cheng, H., 2015. The earliest unequivocally modern humans in southern China. *Nature* 526, 696–699. <https://doi.org/10.1038/nature15696>.
- Liu, X.M., Liu, Z., Lu, B., Markovic, S.B., Chen, J.S., Guo, H., Ma, M.M., Zhao, G.Y., Feng, H., 2013. The magnetic properties of Serbian loess and its environmental significance. *Chin. Sci. Bull.* 58, 353–363. <https://doi.org/10.1007/s11434-1102-1538-11439>.
- Liu, Z., Otto-Blienes, B., He, F., Brady, E., Tomas, R., Clark, P., Carlson, A., Lynch-Stieglitz, J., Curry, W., Brook, E., 2009. Transient simulation of last deglaciation with a new mechanism for Bølling-Allerød warming. *Science* 325, 310–314. <https://doi.org/10.1126/science.1171041>.
- Lo, L., Belt, S.T., Lattaud, J., Friedrich, T., Zeeden, C., Schouten, S., Smik, L., Timmermann, A., Cabedo-Sanz, P., Huang, J.-J., 2018. Precession and atmospheric CO₂ modulated variability of sea ice in the central Okhotsk Sea since 130,000 years ago. *Earth Planet Sci. Lett.* 488, 36–45. <https://doi.org/10.1016/j.epsl.2018.1002.1005>.
- Lu, H., Jia, J., Yin, Q., Xia, D., Gao, F., Liu, H., Fan, Y., Li, Z., Wang, X., Berger, A., 2020. Atmospheric dynamics patterns in southern central Asia since 800 ka revealed by loess-paleosol sequences in Tajikistan. *Geophys. Res. Lett.* 47, e2020GL088320. <https://doi.org/10.081029/082020GL088320>.
- Lu, H., Zhou, Y., Liu, W., Mason, J., 2012. Organic stable carbon isotopic composition reveals late Quaternary vegetation changes in the dune fields of northern China. *Quat. Res.* 77, 433–444. <https://doi.org/10.1016/j.yqres.2012.1001.1009>.
- Lu, H.X., Liu, W.G., Yang, H., Wang, H.Y., Liu, Z.H., Leng, Q., Sun, Y.B., Zhou, W.J., An, Z.S., 2019. 800-kyr land temperature variations modulated by vegetation changes on Chinese Loess Plateau. *Nat. Commun.* 10, 1958. <https://doi.org/10.1038/s41467-41019-09978-41461>.

- Lu, H.Y., An, Z.S., 1997. Pretreatment methods in loess-palaeosol granulometry. *Chin. Sci. Bull.* 42, 237–240.
- Lu, H.Y., Yi, S.W., Liu, Z.Y., Mason, J.A., Jiang, D.B., Cheng, J., Stevens, T., Xu, Z.W., Zhang, E.L., Jin, L.Y., Zhang, Z.H., Guo, Z.T., Wang, Y., Otto-Biesner, B., 2013. Variation of East Asian monsoon precipitation during the past 21 k.y. and potential CO₂ forcing. *Geology* 41, 1023–1026. <https://doi.org/10.1130/G34488.34481>.
- Lu, J., Chen, G., Frierson, D.M., 2010. The position of the midlatitude storm track and eddy-driven westerlies in aquaplanet AGCMs. *J. Atmos. Sci.* 67, 3984–4000. <https://doi.org/10.1175/2010JAS3477.1>.
- Lützow, M.v., Kögel-Knabner, I., Ekschmitt, K., Matzner, E., Guggenberger, G., Marschner, B., Flessa, H., 2006. Stabilization of organic matter in temperate soils: mechanisms and their relevance under different soil conditions—a review. *Eur. J. Soil Sci.* 57, 426–445. <https://doi.org/10.1111/j.1365-2389.2006.00809.x>.
- Lydolph, P.E., 1977. *Climates of the Soviet Union, World Survey of Climatology*. Elsevier, Amsterdam.
- Ma, S., Chen, S., Chen, J., Chen, J., Cao, D., Xoplaki, E., Luterbacher, J., Chen, F., Huang, W., 2025. The Holocene precipitation dipole pattern in the Asian drylands: mechanisms and processes from PMIP4 simulations and paleo-proxy evidence. *Quat. Sci. Rev.* 347, 109091. <https://doi.org/10.101016/j.quascirev.202024.109091>.
- Mackiewicz, A., Ratajczak, W., 1993. Principal components analysis (PCA). *Comput. Geosci.* 19, 303–342. [https://doi.org/10.101016/0098-3004\(1093\)90090-R](https://doi.org/10.101016/0098-3004(1093)90090-R).
- Maher, B.A., 1998. Magnetic properties of modern soils and Quaternary loessic paleosols: paleoclimatic implications. *Palaeogeogr. Palaeoclimatol. Palaeoecol.* 137, 25–54. [https://doi.org/10.1016/S0031-0182\(1097\)00103-X](https://doi.org/10.1016/S0031-0182(1097)00103-X).
- Maher, B.A., Taylor, R.M., 1988. Formation of ultrafine-grained magnetite in soils. *Nature* 336, 368–370. <https://doi.org/10.1038/336368a336360>.
- Mantsis, D.F., Clement, A.C., Broccoli, A.J., Erb, M.P., 2011. Climate feedbacks in response to changes in obliquity. *J. Clim.* 24, 2830–2845. <https://doi.org/10.1175/2010JCLI3986.2831>.
- Mantsis, D.F., Lintner, B.R., Broccoli, A.J., Erb, M.P., Clement, A.C., Park, H.-S., 2014. The response of large-scale circulation to obliquity-induced changes in meridional heating gradients. *J. Clim.* 27, 5504–5516. <https://doi.org/10.1175/JCLI-D-5513-00521>.
- Martrat, B., Grimaldi, J.O., Shackleton, N.J., de Abreu, L., Hutterli, M.A., Stocker, T.F., 2007. Four climate cycles of recurring deep and surface water destabilizations on the Iberian margin. *Science* 317, 502–507, 510.1126/science.1139994.
- Mehteran, S., Pourmand, A., Sharifi, A., Lahijani, H.A., Naderi, M., Swart, P.K., 2017. Speleothem records of glacial/interglacial climate from Iran forewarn of future Water Availability in the interior of the Middle East. *Quat. Sci. Rev.* 164, 187–198. <https://doi.org/10.1016/j.quascirev.2017.1003.1028>.
- Mejdahl, V., 1987. Internal radioactivity in quartz and feldspar grains. *Ancient TL* 5, 10–17. <https://doi.org/10.26034/la.atl.1987.119>.
- Mellars, P., 2006. Why did modern human populations disperse from Africa ca. 60,000 years ago? A new model. *Proc. Natl. Acad. Sci.* 103, 9381–9386. <https://doi.org/10.1073/pnas.051079210>.
- Meng, X.Q., Liu, L.W., Miao, X.D., Zhao, W.C., Zhang, E.L., Ji, J.F., 2021. Significant influence of Northern Hemisphere high latitude climate on appeared precession rhythm of East Asian summer monsoon after Mid-Brunhes Transition interglacials recorded in the Chinese loess. *Catena* 197, 105002. <https://doi.org/10.101016/j.catena.102020.105002>.
- Meyer-Christoffer, A., Becker, A., Finger, P., Schneider, U., Ziese, M., 2018. GPCC climatology version 2018 at 0.25° Monthly Land-Surface Precipitation Climatology for Every Month and the Total Year from Rain-Gauges Built on GTS-Based and Historical Data. Offenbach, Germany.
- Miao, X., Mason, J.A., Johnson, W.C., Wang, H., 2007. High-resolution proxy record of Holocene climate from a loess section in Southwestern Nebraska, USA. *Palaeogeogr. Palaeoclimatol. Palaeoecol.* 245, 368–381. <https://doi.org/10.1016/j.palaeo.2006.1009.1004>.
- Miao, Y., Herrmann, M., Wu, F., Yan, X., Yang, S., 2012. What controlled mid-late miocene long-term aridification in central Asia?—global cooling or Tibetan plateau uplift: a review. *Earth Sci. Rev.* 112, 155–172. <https://doi.org/10.1016/j.earscirev.2012.1002.1003>.
- Miao, Y., Song, Y., Li, Y., Yang, S., Li, Y., Zhao, Y., Zeng, M., 2020. Late Pleistocene fire in the Ili Basin, Central Asia, and its potential links to paleoclimate change and human activities. *Palaeogeogr. Palaeoclimatol. Palaeoecol.* 547, 109700. <https://doi.org/10.1016/j.palaeo.2020.109700>.
- Michel, V., Valladas, H., Shen, G., Wang, W., Zhao, J.-x., Shen, C.-C., Valensi, P., Bae, C. J., 2016. The earliest modern Homo sapiens in China? *J. Hum. Evol.* 101, 101–104. <https://doi.org/10.1016/j.jhevol.2016.07.008>.
- Molnar, P., England, P., 1990. Late cenozoic uplift of mountain-ranges and global climate change - chicken or egg. *Nature* 346, 29–34. <https://doi.org/10.1038/346029a346020>.
- Murata, K.J., Norman, M.B., 1976. An index of crystallinity for quartz. *Am. J. Sci.* 276, 1120–1130. <http://pascal-francis.inist.fr/vibad/index.php?action=getRecordDetail&idt=PASCALGEODEBRGM7720117202>.
- Nilsson-Kerr, K., Anand, P., Holden, P.B., Clemens, S.C., Leng, M.J., 2021. Dipole patterns in tropical precipitation were pervasive across landmasses throughout Marine Isotope Stage 5. *Commun. Earth Environ.* 2, 64. <https://doi.org/10.1038/s43247-43021-00133-43247>.
- Ning, W., Zan, J., Heller, F., Fang, X., Zhang, Y., Zhang, W., Kang, J., Shen, M., 2023. Magnetic proxy of Eurasian loess revealing enhanced physical erosion since the Mid-Pleistocene Transition. *Geophys. Res. Lett.* 50, e2023GL104411. <https://doi.org/10.1029/2023GL104411>.
- Ono, Y., Naruse, T., Ikeya, M., Kohno, H., Toyoda, S., 1998. Origin and derived courses of eolian dust quartz deposited during marine isotope stage 2 in East Asia, suggested by ESR signal intensity. *Global Planet. Change* 18, 129–135. [https://doi.org/10.1016/S0921-8181\(1098\)00012-00015](https://doi.org/10.1016/S0921-8181(1098)00012-00015).
- Orland, I.J., He, F., Bar-Matthews, M., Chen, G., Ayalon, A., Kutzbach, J.E., 2019. Resolving seasonal rainfall changes in the Middle East during the last interglacial period. *Proc. Natl. Acad. Sci.* 116, 24985–24990. <https://doi.org/10.1073/pnas.1903139116>.
- PAGES, P.I.W.G.o., 2016. Interglacials of the last 800,000 years. *Rev. Geophys.* 54, 162–219. <https://doi.org/10.1002/2015RG000482>.
- Pailler, D., Bard, E., 2002. High frequency palaeoceanographic changes during the past 140 000 yr recorded by the organic matter in sediments of the Iberian Margin. *Palaeogeogr. Palaeoclim. Palaeoecol.* 181, 431–452. [https://doi.org/10.1016/S0031-0182\(0100100444-00448](https://doi.org/10.1016/S0031-0182(0100100444-00448).
- Parton, W.J., Schimel, D.S., Cole, C.V., Ojima, D.S., 1987. Analysis of factors controlling soil organic-matter levels in Great-Plains grasslands. *Soil Sci. Soc. America J.* 51, 1173–1179. <https://doi.org/10.2136/sssaj1987.03615995005100050015x>.
- Peng, D., Zhou, T., Zhang, L., Zou, L., 2019. Detecting human influence on the temperature changes in Central Asia. *Clim. Dyn.* 53, 4553–4568. <https://doi.org/10.1007/s00382-019-04804-2>.
- Petit, J.-R., Jouzel, J., Raynaud, D., Barkov, N.I., Barnola, J.-M., Basile, I., Bender, M., Chappellaz, J., Davis, M., Delaygue, G., 1999. Climate and atmospheric history of the past 420,000 years from the Vostok ice core, Antarctica. *Nature* 399, 429–436. <https://doi.org/10.1038/20859>.
- Petraglia, M., Korisettar, R., Boivin, N., Clarkson, C., Ditchfield, P., Jones, S., Koshy, J., Lahr, M.M., Oppenheimer, C., Pyle, D., 2007. Middle Paleolithic assemblages from the Indian subcontinent before and after the Toba super-eruption. *Science* 317, 114–116. <https://doi.org/10.1126/science.114156>.
- Prescott, J.R., Hutton, J.T., 1994. Cosmic ray contributions to dose rates for luminescence and ESR dating: large depths and long-term time variations. *Radiat. Meas.* 23, 497–500. [https://doi.org/10.1016/1350-4487\(1094\)90086-90088](https://doi.org/10.1016/1350-4487(1094)90086-90088).
- Qiang, M., Lang, L., Wang, Z., 2010. Do fine-grained components of loess indicate westerlies: insights from observations of dust storm deposits at Lenghu (Qaidam Basin, China). *J. Arid Environ.* 74, 1232–1239. <https://doi.org/10.1016/j.jaridenv.2010.1206.1002>.
- R Core Team, 2019. R: A Language and Environment for Statistical Computing. R Foundation for Statistical Computing, Vienna, Austria. Retrieved from. <https://www.R-project.org/>.
- Rao, Z., Wu, D., Shi, F., Guo, H., Cao, J., Chen, F., 2019. Reconciling the ‘westerlies’ and ‘monsoon’ models: a new hypothesis for the Holocene moisture evolution of the Xinjiang region, NW China. *Earth Sci. Rev.* 191, 263–272. <https://doi.org/10.1016/j.earscirev.2019.03.002>.
- Rao, Z., Xu, Y., Xia, D., Xie, L., Chen, F., 2013. Variation and paleoclimatic significance of organic carbon isotopes of Ili loess in arid Central Asia. *Org. Geochem.* 63, 56–63. <https://doi.org/10.1016/j.orggeochem.2013.08.007>.
- Rodríguez-Sanz, L., Bernasconi, S.M., Marino, G., Heslop, D., Mueller, I.A., Fernández, A., Grant, K.M., Rohling, E.J., 2017. Penultimate deglacial warming across the Mediterranean Sea revealed by clumped isotopes in foraminifera. *Sci. Rep.* 7, 16572. <https://doi.org/10.1038/s41598-017-16528-6>.
- Rodríguez-Zuriturbe, I., Dotorico, P., Porporato, A., Ridolfi, L., 1999. On the spatial and temporal links between vegetation, climate, and soil moisture. *Water Resour. Res.* 35, 3709–3722, 10.1029/1999WR900255.
- Routson, C.C., McKay, N.P., Kaufman, D.S., Erb, M.P., Goosse, H., Shuman, B.N., Rodysill, J.R., Ault, T., 2019. Mid-latitude net precipitation decreased with Arctic warming during the Holocene. *Nature* 568, 83–87. <https://doi.org/10.1038/s41586-41019-41060-41583>.
- Rugenstein, J.K.C., Chamberlain, C.P., 2018. The evolution of hydroclimate in Asia over the Cenozoic: a stable-isotope perspective. *Earth Sci. Rev.* 185, 1129–1156. <https://doi.org/10.1016/j.earscirev.2018.09.003>.
- Runge, J., Bathiany, S., Bollett, E., Camps-Valls, G., Coumou, D., Doyle, E., Glymour, C., Kretschmer, M., Mahecha, M., Muñoz-Marí, J., 2019. Inferring causation from time series in Earth system sciences. *Nat. Commun.* 10, 2553. <https://doi.org/10.1038/s41467-41019-10105-41463>.
- Sadori, L., Koutsoudensis, A., Panagiotopoulos, K., Masi, A., Bertini, A., Combourieu-Nebout, N., Francke, A., Kouli, K., Joannin, S., Mercuri, A.M., 2016. Pollen-based paleoenvironmental and paleoclimatic change at Lake Ohrid (south-eastern Europe) during the past 500 ka. *Biogeosciences* 13, 1423–1437. <https://doi.org/10.5194/bg-1413-1423-2016>.
- Schaebeitz, F., Asrat, A., Lamb, H.F., Cohen, A.S., Foerster, V., Duesing, W., Kaboth-Bahr, S., Opitz, S., Viehberg, F.A., Vogelsang, R., 2021. Hydroclimate changes in eastern Africa over the past 200,000 years may have influenced early human dispersals. *Commun. Earth Environ.* 2, 123. <https://doi.org/10.1038/s43247-021-00195-7>.
- Schneider, R., Almqvist, B., Svedlindh, P., Hedlund, D., Thyr, J., Kurbanov, R., Stevens, T., 2025. The more the merrier—multi-frequency magnetic susceptibility of loess and paleosols as a sensitive climate proxy. *J. Geophys. Res. Solid Earth* 130, e2024JB029727. <https://doi.org/10.1029/2024JB029727>.
- Scussolini, P., Bakker, P., Guo, C., Stepanek, C., Zhang, Q., Bracconnot, P., Cao, J., Guarino, M.-V., Coumou, D., Prange, M., 2019. Agreement between reconstructed and modeled boreal precipitation of the Last Interglacial. *Sci. Adv.* 5, eaax7047. <https://doi.org/10.1126/sciadv.aax7047>.
- Sha, Y., Shi, Z., Hou, Y., Mao, X., 2023. Modeling studies on the impacts of the Hindu Kush mountains and Iranian plateau on the climate evolution in monsoonal south Asia and central Asia. *Quat. Sci.* 43, 925–939. <https://doi.org/10.11288/j.issn.1001-7410.2023.04.02> (in Chinese with English abstract).
- Sha, Y.Y., Shi, Z.G., Liu, X.D., An, Z.S., Li, X.Z., Chang, H., 2018. Role of the tian Shan mountains and Pamir Plateau in increasing spatiotemporal differentiation of

- precipitation over interior Asia. *J. Clim.* 31, 8141–8162. <https://doi.org/10.1175/JCLI-D-8117-0594.8141>.
- Shackleton, N.J., An, Z., Dodonov, A.E., Gavin, J., Kukla, G.J., Ranov, V.A., Zhou, L., 1995. Accumulation rate of loess in Tadzhikistan and China: relationship with global ice volume cycles. In: Derbyshire, E. (Ed.), *Wind Blown Sediments in the Quaternary Record. Quaternary Proceedings*. Wiley, Chichester, pp. 1–6, 1995.
- Shakun, J.D., Lea, D.W., Lisicki, L.E., Raymo, M.E., 2015. An 800-kyr record of global surface ocean δ₁₈O and implications for ice volume-temperature coupling. *Earth Planet Sci. Lett.* 426, 58–68. <https://doi.org/10.1016/j.epsl.2015.05.042>.
- Shi, C.D., Zhu, R.X., Glass, B.P., Liu, Q.S., Zeman, A., Suchy, V., 2003. Climate variations since the last interglacial recorded in Czech loess. *Geophys. Res. Lett.* 30. <https://doi.org/10.1029/2003GL017251>.
- Smalley, I.J., Kumar, R., Dhand, K.O., Jefferson, I.F., Evans, R.D., 2005. The formation of silt material for terrestrial sediments: particularly loess and dust. *Sediment. Geol.* 179, 321–328. <https://doi.org/10.1016/j.sedgeo.2005.06.011>.
- Snyder, C.W., 2016. Evolution of global temperature over the past two million years. *Nature* 538, 226–228. <https://doi.org/10.1038/nature19798>.
- Song, Y., Li, Y., Cheng, L., Zong, X., Kang, S., Ghafarpour, A., Li, X., Sun, H., Fu, X., Dong, J., 2021. Spatio-temporal distribution of quaternary loesses across central Asia. *Palaeogeogr. Palaeoclimatol. Palaeoecol.* 567, 110279. <https://doi.org/10.1016/j.palaeo.2021.110279>.
- Sproson, A.D., Yokoyama, Y., Miyairi, Y., Aze, T., Clementi, V.J., Riechelson, H., Bova, S. C., Rosenthal, Y., Childress, L.B., 2024. Near-synchronous northern Hemisphere and patagonian ice sheet variation over the last glacial cycle. *Nat. Geosci.* 17, 450–457. <https://doi.org/10.1038/s41561-024-01436-y>.
- Stevens, T., Buylaert, J.-P., Thiel, C., Újvári, G., Yi, S., Murray, A., Frechen, M., Lu, H., 2018. Ice-volume-forced erosion of the Chinese Loess Plateau global Quaternary stratotype site. *Nat. Commun.* 9, 983. <https://doi.org/10.1038/s41467-41018-0329-41462>.
- Stockhecke, M., Timmermann, A., Kipfer, R., Haug, G.H., Kwiecien, O., Friedrich, T., Menviel, L., Litt, T., Pickarski, N., Anselmetti, F.S., 2016. Millennial to orbital-scale variations of drought intensity in the Eastern Mediterranean. *Quat. Sci. Rev.* 133, 77–95. <https://doi.org/10.1016/j.quascirev.2015.1012.1016>.
- Su, Y., Chen, S., Li, X., Ma, S., Xie, T., Wang, J., Yan, D., Chen, J., Feng, M., Chen, F., 2023. Changes in vegetation greenness and its response to precipitation seasonality in Central Asia from 1982 to 2022. *Environ. Res. Lett.* 18, 104002. <https://iopscience.iop.org/article/104010.101088/101748-109326/acf104058e>.
- Sugihara, G., 1994. Nonlinear forecasting for the classification of natural time series. *Philos. Trans. R. Soc. Lond. Series A. Phys. Eng. Sci.* 348, 477–495. <https://doi.org/10.1098/rsta.1994.0106>.
- Sugihara, G., May, R., Ye, H., Hsieh, C.-h., Deyle, E., Fogarty, M., Munch, S., 2012. Detecting causality in complex ecosystems. *Science* 338, 496–500, 410.1126/science.122707.
- Sun, D., Su, R., Li, Z., Lu, H., 2011a. The ultrafine component in Chinese loess and its variation over the past 7–6 Ma: implications for the history of pedogenesis. *Sedimentology* 58, 916–935. <https://doi.org/10.1111/j.1365-3091.2010.01189.x>.
- Sun, Y., Chen, H., Tada, R., Weiss, D., Lin, M., Toyoda, S., Yan, Y., Isozaki, Y., 2013. ESR signal intensity and crystallinity of quartz from Gobi and sandy deserts in East Asia and implication for tracing Asian dust provenance. *Geochim. Geophys. Geosyst.* 14, 2615–2627. <https://doi.org/10.1002/ggge.20162>.
- Sun, Y., McManus, J.F., Clemens, S.C., Zhang, X., Vogel, H., Hodell, D.A., Guo, F., Wang, T., Liu, X., An, Z., 2021. Persistent orbital influence on millennial climate variability through the Pleistocene. *Nat. Geosci.* 14, 812–818. <https://doi.org/10.1038/s41561-4102-00794-41561>.
- Sun, Y., Tada, R., Chen, J., Chen, H., Toyoda, S., Tani, A., Isozaki, Y., Nagashima, K., Hasegawa, H., Ji, J., 2007. Distinguishing the sources of Asian dust based on electron spin resonance signal intensity and crystallinity of quartz. *Atmos. Environ.* 41, 8537–8548. <https://doi.org/10.1016/j.atmosenv.2007.8507.8014>.
- Sun, Y., Tada, R., Chen, J., Liu, Q., Toyoda, S., Tani, A., Ji, J., Isozaki, Y., 2008. Tracing the provenance of fine-grained dust deposited on the central Chinese Loess Plateau. *Geophys. Res. Lett.* 35, L01804. <https://doi.org/10.1029/2007GL031672>.
- Sun, Y.B., He, L., Liang, L.J., An, Z.S., 2011b. Changing color of Chinese loess: geochemical constraint and paleoclimatic significance. *J. Asian Earth Sci.* 40, 1131–1138. <https://doi.org/10.1016/j.jseas.2010.1108.1006>.
- Takens, F., 1981. Detecting strange attractors in turbulence. In: Rand, D., Young, L.S. (Eds.), *Dynamical Systems and Turbulence Warwick 1980. Lecture Notes in Mathematics*. Springer, Berlin Heidelberg, pp. 366–381.
- Tan, L., Cheng, H., Li, D., Orozbaev, R., Li, Y., Xu, H., Edwards, R.L., Song, Y., Ma, L., Lin, F., 2024. Hydroclimatic changes on multiple timescales since 7800 y BP in the winter precipitation-dominated Central Asia. *Proc. Natl. Acad. Sci.* 121, e2321645121. <https://doi.org/10.23216/14073/pnas.2321645121>.
- Thiel, C., Buylaert, J.-P., Murray, A., Terhorst, B., Hofer, I., Tsukamoto, S., Frechen, M., 2011a. Luminescence dating of the Stratzing loess profile (Austria)—Testing the potential of an elevated temperature post-IR IRSL protocol. *Quat. Int.* 234, 23–31. <https://doi.org/10.1016/j.quaint.2010.1005.1018>.
- Thiel, C., Buylaert, J.-P., Murray, A.S., Tsukamoto, S., 2011b. On the applicability of post-IR IRSL dating to Japanese loess. *Geochronometria* 38, 369–378. <https://doi.org/10.2478/s13386-13011-10043-13384>.
- Thomsen, K.J., Murray, A.S., Jain, M., Bøtter-Jensen, L., 2008. Laboratory fading rates of various luminescence signals from feldspar-rich sediment extracts. *Radiat. Meas.* 43, 1474–1486. <https://doi.org/10.1016/j.radmeas.2008.1406.1002>.
- Tian, S., Sun, J., Zhang, Z., Abdulov, S., Cao, M., Gadeev, M., Oimahmadov, I., 2021. Loess deposits in the Tajik basin, central Asia: chronology, provenance and palaeoclimatic implications since the last glacial. *Boreas* 50, 147–166. <https://doi.org/10.1111/bor.12467>.
- Tierney, J.E., Poulsen, C.J., Montañez, I.P., Bhattacharya, T., Feng, R., Ford, H.L., Hönnisch, B., Inglis, G.N., Petersen, S.V., Sagoo, N., 2020. Past climates inform our future. *Science* 370, eaay3701. <https://www.science.org/doi/abs/3710.1126/science.aay3701>.
- Timmermann, A., Friedrich, T., 2016. Late Pleistocene climate drivers of early human migration. *Nature* 538, 92–95. <https://doi.org/10.1038/nature19365>.
- Timmermann, A., Friedrich, T., Timm, O.E., Chikamoto, M.O., Abe-Ouchi, A., Ganopolski, A., 2014. Modeling obliquity and CO₂ effects on Southern Hemisphere climate during the past 408 ka. *J. Clim.* 27, 1863–1875. <https://doi.org/10.1175/JCLI-D-13-00311.1>.
- Timmermann, A., Yun, K.-S., Raia, P., Ruan, J., Mondanaro, A., Zeller, E., Zollikofer, C., Ponc de León, M., Lemmon, D., Willeit, M., 2022. Climate effects on archaic human habitats and species successions. *Nature* 604, 495–501. <https://doi.org/10.1038/s41586-022-04600-9>.
- Torrent, J., Schwertmann, U., Fechter, H., Alferez, F., 1983. Quantitative relationships between soil color and hematite content. *Soil Sci.* 136, 354–358. https://journals.lww.com/soilsci/abstract/1983/12000/Quantitative_Relationships_Between_Soil_Colour_and_4.aspx.
- Tsonis, A.A., Deyle, E.R., May, R.M., Sugihara, G., Swanson, K., Verbeten, J.D., Wang, G., 2015. Dynamical evidence for causality between galactic cosmic rays and interannual variation in global temperature. *Proc. Natl. Acad. Sci.* 112, 3253–3256. <https://doi.org/10.1073/pnas.1420291112>.
- Újvári, G., Schneider, R., Stevens, T., Rinyu, L., Kiss, G.I., Buylaert, J.-P., Murray, A.S., Challier, A.J., Kurbanov, R., Khormali, F., 2024. Absolute 230Th/U chronologies and Δ47 thermometry paleoclimate reconstruction from soil carbonates in Central Asian loess over the past 1 million years. *Geochem. Cosmochim. Acta* 386, 110–126. <https://doi.org/10.1016/j.gca.2024.09.008>.
- Van der Meerens, T., Verschuren, D., Sylvestre, F., Nassour, Y.A., Naudts, E.L., Aguilar Ortiz, L.E., Deschamps, P., Tachikawa, K., Bard, E., Schuster, M., 2022. A predominantly tropical influence on late Holocene hydroclimate variation in the hyperarid central Sahara. *Sci. Adv.* 8, eabk1261. <https://doi.org/10.1126/sciadv.eabk1261>.
- Van Nes, E.H., Scheffer, M., Brovkin, V., Lenton, T.M., Ye, H., Deyle, E., Sugihara, G., 2015. Causal feedbacks in climate change. *Nat. Clim. Change* 5, 445–448. <https://doi.org/10.1038/nclimate2568>.
- Vandenberge, J., 2013. Grain size of fine-grained windblown sediment: a powerful proxy for process identification. *Earth Sci. Rev.* 121, 18–30. <https://doi.org/10.1016/j.earscirev.2013.1003.1001>.
- Wang, L., Jia, J., Li, G., Li, Z., Wang, X., Chen, F., 2018a. Fine-grained quartz OSL dating chronology of loess sequence from southern Tajikistan: implications for climate change in arid central Asia during MIS 2. *J. Asian Earth Sci.* 155, 116–123. <https://doi.org/10.1016/j.jseas.2017.11.001>.
- Wang, Q., Tang, X., Lei, J., Jia, J., Murodov, D., Wang, B., Yao, Z., Wang, X., Chen, J., 2024. Paleoclimatic significance of the organic carbon isotopes of the Tajikistan loess in arid Central Asia, on orbital timescales since the last interglacial. *Palaeogeogr. Palaeoclimatol. Palaeoecol.* 653, 112425. <https://doi.org/10.1016/j.palaeo.2024.112425>.
- Wang, X., Piao, S., Ciais, P., Friedlingstein, P., Myneni, R.B., Cox, P., Heimann, M., Miller, J., Peng, S., Wang, T., 2014. A two-fold increase of carbon cycle sensitivity to tropical temperature variations. *Nature* 506, 212–215. <https://doi.org/10.1038/nature12915>.
- Wang, X., Sun, D.H., Wang, F., Li, B.F., Wu, S., Guo, F., Li, Z.J., Zhang, Y.B., Chen, F.H., 2013. A high-resolution multi-proxy record of late Cenozoic environment change from central Taklimakan Desert, China. *China. Clim. Past* 9, 2731–2739. <https://doi.org/10.5194/cp-2739-2731-2013>.
- Wang, Y., Cheng, H., Edwards, R.L., Kong, X., Shao, X., Chen, S., Wu, J., Jiang, X., Wang, X., An, Z., 2008. Millennial-and orbital-scale changes in the East Asian monsoon over the past 224,000 years. *Nature* 451, 1090–1093. <https://doi.org/10.1038/nature06692>.
- Wang, Y., Jia, J., Liu, H., Lu, C., Xia, D., Lu, H., 2018b. The magnetic susceptibility recorded millennial-scale variability in central Asia during last glacial and interglacial. *Geophys. J. Int.* 215, 1781–1788. <https://doi.org/10.1093/gji/ggy1378>.
- Wang, Y., Yang, J., Chen, Y., De Maeyer, P., Li, Z., Duan, W., 2018c. Detecting the causal effect of soil moisture on precipitation using convergent cross mapping. *Sci. Rep.* 8, 12171. <https://doi.org/10.1038/s41598-018-30669-2>.
- Wang, Y., Larsen, T., Lauterbach, S., Andersen, N., Blanz, T., Krebs-Kanzow, U., Gierz, P., Schneider, R.R., 2022. Higher sea surface temperature in the Indian ocean during the last interglacial weakened the South Asian monsoon. *Proc. Natl. Acad. Sci.* 119, e2107720119. <https://doi.org/10.1073/pnas.2107720119>.
- Westaway, K.E., Louys, J., Awe, R.D., Morwood, M.J., Price, G.J., Zhao, J.-x., Aubert, M., Joannes-Boyau, R., Smith, T., Skinner, M.M., 2017. An early modern human presence in Sumatra 73,000–63,000 years ago. *Nature* 548, 322–325. <https://doi.org/10.1038/nature23452>.
- Wintle, A.G., Murray, A.S., 2006. A review of quartz optically stimulated luminescence characteristics and their relevance in single-aliquot regeneration dating protocols. *Radiat. Meas.* 41, 369–391. <https://doi.org/10.1016/j.radmeas.2005.1011.1001>.
- Wiscombe, W.J., 1980. Improved Mie scattering algorithms. *Appl. Opt.* 19, 1505–1509. <https://doi.org/10.1364/AO.19.001505>.
- Wood, S., Wood, M.S., 2015. Package 'mgcv'. R package version 1, 729.
- Wu, G., Yao, T., Xu, B., Li, Z., Tian, L., Duan, K., Wen, L., 2006. Grain size record of microparticles in the Muztagata ice core. *Sci. China Earth Sci.* 49, 10–17. <https://doi.org/10.1007/s11430-11004-15093-11435>.
- Xiao, J., Nakamura, T., Lu, H., Zhang, G., 2002. Holocene climate changes over the desert/loess transition of north-central China. *Earth Planet Sci. Lett.* 197, 11–18. [https://doi.org/10.1016/S0012-1821\(02\)00463-0](https://doi.org/10.1016/S0012-1821(02)00463-0).

- Yang, H., Li, G., Huang, X., Wang, X., Zhang, Y., Jonell, T.N., Jin, M., Chen, C., Zhao, W., Zhang, H., 2020a. Loess depositional dynamics and paleoclimatic changes in the Yili Basin, Central Asia, over the past 250 ka. *Catena* 195, 104881. <https://doi.org/10.101016/j.catena.102020.104881>.
- Yang, L., Jia, J., 2021. Temperature dependence of pedogenic magnetic mineral formation in loess deposits. *Quat. Int.* 580, 95–99. <https://doi.org/10.101016/j.quaint.2021.1001.1022>.
- Yang, S., Ding, F., Ding, Z., 2006. Pleistocene chemical weathering history of Asian arid and semi-arid regions recorded in loess deposits of China and Tajikistan. *Geochem. Cosmochim. Acta* 70, 1695–1709. <https://doi.org/10.101016/j.gca.2005.1612.1012>.
- Yang, S., Ding, Z., 2006. Winter-spring precipitation as the principal control on predominance of C3 plants in Central Asia over the past 1.77 Myr: evidence from δ13C of loess organic matter in Tajikistan. *Palaeoclim. Palaeoecol.* 235, 330–339. <https://doi.org/10.101016/j.palaeo.2005.11.007>.
- Yang, S., Fang, X., Li, J., An, Z., Chen, S., Hitoshi, F., 2001. Transformation functions of soil color and climate. *Sci. China Earth Sci.* 44, 218–226. <https://doi.org/10.1007/BF02911990>.
- Yang, S., Li, D., Liu, N., Zan, J., Liu, W., Kang, J., Murodov, A., Fang, X., 2020b. Quartz optically stimulated luminescence dating of loess in Tajikistan and its paleoclimatic implications for arid Central Asia since the Lateglacial. *Palaeogeogr. Palaeoclimatol. Palaeoecol.* 556, 109881. <https://doi.org/10.101016/j.palaeo.102020.109881>.
- Yang, S.L., Ding, Z.L., 2003. Color reflectance of Chinese loess and its implications for climate gradient changes during the last two glacial-interglacial cycles. *Geophys. Res. Lett.* 30. <https://doi.org/10.1029/2003GL018346>.
- Yao, Z., Shi, X., Yin, Q., Jaccard, S., Liu, Y., Guo, Z., Gorbarenko, S.A., Wang, K., Chen, T., Wu, Z., 2024. Ice sheet and precession controlled subarctic Pacific productivity and upwelling over the last 550,000 years. *Nat. Commun.* 15, 3489. <https://doi.org/10.1038/s41467-024-47871-8>.
- Ye, H., Clark, A., Deyle, E., Munch, S., Keyes, O., Cai, J., White, E., Cowles, J., Stagge, J., Daon, Y., 2018. rEDM: Applications of empirical dynamic modeling from time series. R package version 0.7.1.
- Ye, H., Deyle, E.R., Gilarranz, L.J., Sugihara, G., 2015. Distinguishing time-delayed causal interactions using convergent cross mapping. *Sci. Rep.* 5, 14750. <https://doi.org/10.11038/srep.14750>.
- Yin, A., Nie, S., Craig, P., Harrison, T., Ryerson, F., Xianglin, Q., Geng, Y., 1998. Late Cenozoic tectonic evolution of the southern Chinese Tian Shan. *Tectonics* 17, 1–27. <https://doi.org/10.1029/97TC03140>.
- Yin, G., Hu, Z., Chen, X., Tiyip, T., 2016. Vegetation dynamics and its response to climate change in Central Asia. *J. Arid Land* 8, 375–388. <https://doi.org/10.1007/s40333-016-0043-6>.
- Yin, Q., Berger, A., 2015. Interglacial analogues of the Holocene and its natural near future. *Quat. Sci. Rev.* 120, 28–46. <https://doi.org/10.101016/j.quascirev.2015.1004.1008>.
- Zaady, E., Offer, Z.Y., Shachak, M., 2001. The content and contributions of deposited aeolian organic matter in a dry land ecosystem of the Negev Desert, Israel. *Atmos. Environ.* 35, 769–776. [https://doi.org/10.101016/S1352-2310\(1000\)00263-00266](https://doi.org/10.101016/S1352-2310(1000)00263-00266).
- Zan, J., Louys, J., Dennell, R., Petraglia, M., Ning, W., Fang, X., Zhang, W., Hu, Z., 2024. Mid-Pleistocene aridity and landscape shifts promoted Palearctic hominin dispersals. *Nat. Commun.* 15, 10279. <https://doi.org/10.1038/s41467-024-54767-0>.
- Zan, J., Ning, W., Heller, F., Fang, X., Zhang, W., Kang, J., 2022. Intensified Northern Hemisphere glaciation facilitates continuous accumulation of late Pliocene loess on the western margin of the Pamir. *Geophys. Res. Lett.* 49, e2022GL099629. <https://doi.org/10.1091029/092022GL099629>.
- Zhang, Y.B., Sun, D.H., Li, Z.J., Wang, F., Wang, X., Li, B.F., Guo, F., Wu, S., 2014. Cenozoic record of aeolian sediment accumulation and aridification from Lanzhou, China, driven by Tibetan Plateau uplift and global climate. *Global Planet. Change* 120, 1–15. <https://doi.org/10.101016/j.gloplacha.2014.1005.1009>.
- Zhao, J., Chen, H., Song, Y., Sun, Y., 2012. Determination of quartz content and crystallinity index from loess samples. *Mar. Geol. Quat. Geol.* 32, 131–135, 110.3724/SP.J1140.2012.05131 (In Chinese with English Abstract). DOI: 10.3724/SP.J1140.2012.05131.
- Zhao, H., Li, S.H., 2005. Internal dose rate to K-feldspar grains from radioactive elements other than potassium. *Radiat. Meas.* 40, 84–93. <https://doi.org/10.101016/j.radmeas.2004.11.004>.
- Zhong, Y., Liu, Y., Yang, H., Yin, Q., Wilson, D.J., Lu, Z., Jaccard, S.L., Struve, T., Clift, P. D., Kaboth-Bahr, S., 2024a. Orbital controls on North Pacific dust flux during the late quaternary. *Geophys. Res. Lett.* 51, e2023GL106631. <https://doi.org/10.1029/2023GL106631>.
- Zhong, Y., Lu, Z., Kaboth-Bahr, S., Yu, J., Horikawa, K., Dekkers, M.J., Larrasoña, J.C., Clift, P.D., Weber, M.E., Vermassen, F., 2025. Precession modulates the poleward expansion of atmospheric circulation to the Arctic Ocean. *Nat. Commun.* 16, 1143. <https://doi.org/10.1038/s41467-025-56542-1>.
- Zhong, Y., Tan, N., Abell, J.T., Sun, C., Kaboth-Bahr, S., Ford, H.L., Herbert, T.D., Pullen, A., Horikawa, K., Yu, J., 2024b. Role of land-ocean interactions in stepwise northern Hemisphere glaciation. *Nat. Commun.* 15, 6711. <https://doi.org/10.1038/s41467-41024-51127-w>.
- Zhou, L.P., Oldfield, F., Wintle, A.G., Robinson, S.G., Wang, J.T., 1990. Partly pedogenic origin of magnetic variations in Chinese loess. *Nature* 346, 737–739. <https://doi.org/10.1038/346737a346730>.
- Zhou, P., Shi, Z.G., Li, X.Z., Zhou, W.J., 2020. Response of westerly jet over the northern Hemisphere to astronomical insolation during the holocene. *Front. Earth Sci.* 8. <https://doi.org/10.3389/feart.2020.00282>.
- Zwyns, N., Paine, C.H., Tsedendorj, B., Talamo, S., Fitzsimmons, K.E., Gantumur, A., Guunii, L., Davakhuu, O., Flas, D., Dogandžić, T., 2019. The northern route for human dispersal in Central and Northeast Asia: new evidence from the site of Tolbor-16, Mongolia. *Sci. Rep.* 9, 11759. <https://doi.org/10.1038/s41598-019-47972-1>.